# Production and characterisation of 3D printed micro-lenses.

THESIS

submitted in partial fulfillment of the
requirements for the degree of

BACHELOR OF SCIENCE
in
PHYSICS


| | |
|---|---|
| Author : | J. M. de Gier |
| Student ID : | s1619179 |
| Supervisor : | M. P. van Exter |
| $2^{nd}$ corrector : | C. U. Keller |


Leiden, The Netherlands, June 18, 2019

# Production and characterisation of 3D printed micro-lenses.

**J. M. de Gier**

Huygens-Kamerlingh Onnes Laboratory, Leiden University
P.O. Box 9500, 2300 RA Leiden, The Netherlands

June 18, 2019

## Abstract

In this thesis we explored various characterisation techniques that can be used to analyse lenses, including the characterisation of a focus and the characterisation of spherical aberration. We used these techniques to analyse two near perfect lenses. We also designed and analysed seven lenses that were printed using the Nanoscribe Photonic Professional GT 3d printer. From this analysis we found that 3d-printed lenses performed as decent lenses. The waist of the focus, produced by the lenses, was smaller than 1 $\mu$m for all lenses. This was within 3 times the diffraction limited waist and the intensity in the focus was up to 360 ($\pm$ 30) times higher than if the lens had not been there. The Strehl ratio of each of the 3d printed lenses has been estimated, which all lie between 0.007 and 0.023. We found that the printed lenses behaved in a predictable manner and even though the micro-lenses show defects under optical inspection, their behaviour is predictable. We attempted to find the limits in quality, quantity and size that can be achieved using the Nanoscribe PPGT and made a beginning in answering this question. We found that micro-lenses created with the Nanoscribe PPGT can be used by the Quantum Optics department to enhance the intensity by acting as solid immersion lenses.

# Contents

Chapter 1

# Introduction

The production of objects that are of interest to society has had an enormous impact on the way our society has shaped itself. From the steam engines of the industrial revolution to current 3d printing, these production methods have changed the limits to what can be produced. Current research in the field of 3d printing would be considered science-fiction no more than 50 years ago. Examples include the ability to print objects such as organs [1] and homes [2].

The Physics department at Leiden university has one such printer, the Nanoscribe Photonic Professional GT (or the Nanoscribe PPGT) created by the German company Nanoscribe. This printer is capable of creating small structures (of the order of $\mu$m to cm). Within the Quantum Optics group the possible applications of 3d printed optical elements for Quantum Optics have hardly been investigated. In this Bachelor's thesis We will discuss the possibilities and limitations of the Nanoscribe PPGT in creating one type of optical structure: micro-lenses.

Micro-lenses are interesting because of the following reasons: They can create a sharp focus by acting as a solid immersion lens (because the size of a focus is inversely proportional to the refractive index); They are small and light and can thus be placed where other lenses can not; And they can be used to focus light on tiny structures by simply placing the lens on top of it (the lens then also works as a solid immersion lens, enhancing the focus). A tiny structure that would benefit from a solid immersion micro-lens is a single photon detector, which M. de Dood is researching in the Quantum Optics group.

A 3d printed structure is unlikely to be exactly as designed, hence altering the behaviour in (un)predictable ways. In this thesis, we will address the following questions:

1. Is it possible to design and print micro-lenses that behave predictably?
2. What are the limits, in quality, quantity and size that can be achieved?

We will try to formulate an answer to these questions, using and creating multiple characterisation techniques.

In chapter two we will briefly discuss 3d printers and how objects are actually printed. In chapter three we will discuss lenses and some parameters that we can use to characterise them. In chapter four we will discuss the experimental setup. In chapter five we will analyse some perfect lenses using the parameters we discussed. In chapter six we will repeat this analysis for some lenses that were printed. Finally in chapter seven we will discuss our findings, draw conclusions and give recommendations. Chapter 8 and 9 contain a step-by-step guide to producing micro-lenses using the Nanoscribe PPTG and mathematical derivations.

Chapter 2

# 3D printing

## 2.1 Possibilities and limitations of 3d printing.

3D printing is a production method in which a material is directly deposited upon a surface in the form of a Voxel (a smallest building block). By repeatedly doing this one can create a structure layer by layer, thus creating a 3d object. 3D printing was invented just three decades ago [3] and has been a growing industry ever since.

Possibilities of 3d printing are that anyone with a 3d printer can create structures of their own design. A wide variety of different materials [4], which possess different properties, are available. This allows one to create an object with highly specific properties. This can be used to even print organs [1] and houses [2]. Commercially available 3d printers [5] are used to create models, toys and other creations. Anyone with a 3d printer and a little practice can now create cheap high quality models that they themselves designed*.

Disadvantages of 3d printing are that it is very difficult to create loose and overarching objects and that a 3d printer works within specific length scales. The problem with creating loose and overarching objects is that it is difficult to print floating objects†, which means that usually one prints from the ground up and every Voxel is connected. There are strategies to work around the problem of loose or overarching objects. Let us examine the example of a ball inside a shell: One can first print the ball and insert it in the shell during its print; A

*A large downside of this is that not everybody is interested in making innocent toys [6]

†For 3d printers that work in air it is impossible to print a floating object, since gravity will ruin everything. 3D printers that work by polymerising a fluid can create floating objects.

second option is printing the ball connected to the shell with a tiny rod that will break off. These strategies won't work in every situation and thus limit what you can create.

We can quantify the quality of a printer in three parameters: Voxel size, precision and minimal step size.

Voxel size in comparison to the size of the object determines the writing time and the resolution. If the object is smaller than the Voxel only a single Voxel is printed (really fast) but it will not look like the object (bad resolution). If the object is small, but somewhat larger, it will be composed of multiple Voxels. The more Voxels that are used the smoother the object will appear (better resolution) but the longer the print takes (longer writing time). Because of this there is an optimum range where the object is not too large and not too small. Because different printers have different Voxel sizes one needs to keep the design size in mind when choosing which printer to use.

Precision is how accurate a Voxel is placed. A printer with a high precision will place its Voxels exactly where its programmed to, while a printer with a low precision will place its Voxels randomly around where its programmed to. Obviously a higher precision is better, but it is impossible to have an infinitely high precision and a higher precision usually comes at the cost of a longer writing time.

Step-size is the distance between two Voxels. The smaller the step size the smoother the object will be, but the longer the writing time. While the step size is adjustable there is a minimum step size that the printer can't physically can get below. This minimum step size is determined by the motors used in the printer and the physical properties of the Voxel (a solid Voxel can't be placed inside another Voxel, but the Nanoscribe uses polymerisation and so it is possible to have the Voxels overlap).

## 2.2 Nanoscribe for 3d printing

Nanoscribe is a German company that created the Nanoscribe Photonic Professional GT (Nanoscribe PPGT). This machine uses two photon polymerisation (2pp) to create 3d printed structures on a microscopic scale [7]. To write these structures, the Nanoscribe, with the 63X lens, uses Voxels which are ellipsoidal blobs with a height of roughly 1 $\mu$m and a diameter of the order of 0.2 $\mu$m (we have been told this by J. Mesman-Vergeer in private communication, Ostendorf [8] and Nanoscribe [9] support this statement).

Two photon polymerisation (2pp) is a technique in which a material consist-

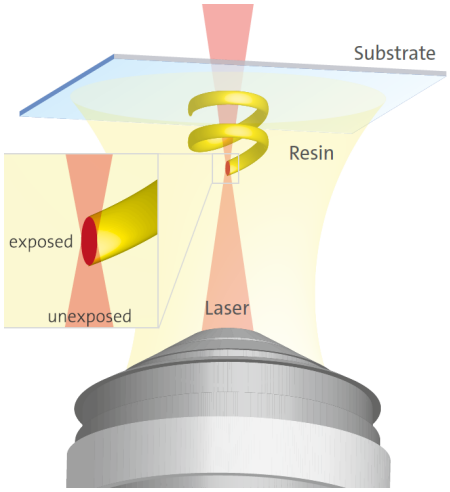


**Figure 2.1:** *The principle of Two photon polymerisation. Figure copied from [7]*

ing of monomers is polymerised through the absorption of two photons. The need to absorb two photons decreases the size of the Voxels. A laser is focused inside of a viscous monomeric material (see figure 2.1) which is mixed with a reagent. The reagent is essentially two parts connected by a single chemical bond:

$$R - R$$

When the reagent is exposed to two photons (or one high energy photon), the bond will break causing two radicals to be formed. They can then start a polymerisation reaction with the surrounding monomers. The reaction is terminated when two radicals react with each other. [10]

Two photon polymerisation uses nonlinear optics to reduce the Voxel size. This works because the probability of absorbing a photon is proportional to the intensity distribution (which is Gaussian). The probability of absorbing two photons at the same time is then proportional to the intensity squared. The intensity squared distribution has a smaller size than that of the normal intensity distribuition, which causes the Voxel size to be smaller than the diffraction limit and thus the quality of the product to be higher. [11]

Nanoscribe states that: "The 3D printers from Nanoscribe are designed as open systems for a broad range of materials" [7]. The materials that Nanoscribe specifically designed for two photon polymerisation are listed in Figure 2.2. Of these materials IP-S and IP-Dip have applications that are specific for micro-optics. We choose to use IP-Dip, as it allows for smaller structures. For light with wavelength 520 nm, the refractive index of IP-Dip is found to be approximately 1.55 [12].

The Nanoscribe PPGT can write in two modes: Piezo and Galvo. In Piezo

| Resin | Advantages | State | Scan speed | Sample size | Resolution | Possible applications |
|---|---|---|---|---|---|---|
| **IP-Q** | High-speed fabrication up to macroscale structures with volumes of tens of mm³. Designed for Dip-in Laser Lithography (DiLL). | Liquid | High | Micro/ Meso/ Macro | Standard | Biomedical engineering, mechanical components, micro rapid prototyping. |
| **IP-S** | Smooth surfaces for micro- and mesoscale fabrication with optical-quality surface roughness and shape accuracy. Designed for Dip-in Laser Lithography (DiLL). | Liquid | High | Micro/ Meso | Medium | Mechanical metamaterials, micro-optics, integrated photonics, microfluidics, cell scaffolds. |
| **IP-Dip** | Submicron features and high aspect ratios. Designed for Dip-in Laser Lithography (DiLL). | Liquid | Medium | Nano/ Micro | High | Photonic metamaterials, diffractive optical elements, microrobots. |
| **IP-G 780** | Complex 3D designs, e.g., overhanging elements. Submicron features and low shrinkage. Designed for oil immersion configuration. | Sol-gel | Medium | Nano/ Micro | High | Overhanging elements in biomimetics, photonics, microrobots. |
| **IP-L 780** | Submicron features and low shrinkage. Designed for oil immersion configuration. Compatible with DiLL. | Liquid | Medium | Nano/ Micro | High | Plasmonics, photonic and biomimetic surfaces. |

**Figure 2.2:** *Overview of the materials provided by Nanoscribe, optimised for two photon polymerization. Figure taken from [7]*

mode the entire substrate is moved with piezos and the laser focus itself doesn't move, while in Galvo mode the substrate remains immobile and the laser focus is moved (using galvo mirrors).

The advantage of Galvo is that it is much faster, allowing for a much shorter writing time. The downsides are that it is generally less precise, it cannot account for tilt in the sample, and it covers a smaller area than Piezo mode.
We will compare structures written in both modes.

The lens that is used to create the focus has an impact on both the quality of the print (through the size of the Voxel) as well as the printing time. There are multiple lenses available, for example the 20X, 25X and 63X lenses. A lens with a higher magnification creates a sharper focus (and thus smaller Voxels), but the print will have a longer writing time. We will use the 63X lens, because it allows for higher quality.

The substrate on which the object is printed also plays a role and there are various options. Two of these are the ITO-coated and fused silica. We will use the fused silica because this is the standard option.

The vertical step size used, in most of our research, was 0.5 $\mu$m. This was indicated to be the standard step size. The horizontal step size was chosen as the standard value of 0.2 $\mu$m (the Voxels do not overlap).

All choices affect each other and it is the combination of lens + substrate + material + writing mode + vertical step size that defines the quality of your print. Not all combinations are practical, for example the fused silica substrate is almost exclusively used in combination with the 63X lens and almost never with the 25X lens (private communication with J. Mesman-Vergeer).

Chapter 3

# Lenses

## 3.1 Short introduction to lenses

A lens is an optical element that bends light depending on where it passes through the lens, which is done by changing the phase front of the light. A perfect lens is often characterised using the working distance WD, focal length $f$ and the numerical aperture NA. Compound lenses, objectives and oculars are also characterised using the magnification $M$.

The *working distance* of a lens is the distance between the focus of the lens and the lens itself if the source of the illumination is placed infinitely far away.

The *focal length* describes how the position of the focus spot changes in the focal plane when a parallel beam illuminates the lens under an angle. $f = dx/d\theta$. For a single thin lens the focal length and working distance are the same and $f$ is used for both.

The *numerical aperture* of a lens is defined as $\text{NA} = n\sin(\theta)$ with $n$ the refractive index of the medium in which the lens is placed (usually air). When the lens is illuminated using a parallel beam $\sin(\theta) \approx \frac{D}{2f}$ where $D$ the diameter of the circular lens and

$$\text{NA} \approx \frac{nD}{2f} \tag{3.1}$$

For an objective $D$ is the maximum diameter of the beam at the exit lens (the effective diameter of the last lens) and $f$ is the working distance.
There is debate about whether $\sin(\theta) \approx D/2f$ or $\tan(\theta) \approx D/2f$ which has to do with the abbe sine condition (see Small [13]). This condition states that for a good objective the sine of the opening angle is $D/2f$ and not the tangent (making equation (3.1) valid for all opening angles). The 3D printed lenses The

measurements performed in this thesis have large enough uncertainties that we can consider the two to be equivalent for all 3d-printed lenses.

For a single lens the *magnification* is defined as the negative of the size of the image divided by the size of the object ($M = -s'/s$). For an objective the magnification is always defined in respect to some tube length (the tube length is the distance between the focal point of the lens and the image , $M = \frac{L_{ref}}{f}$ and $L_{ref}$ depends on the manufacturer.

## 3.2 Aberrations

A real lens has defects which will cause the phase front to be aberrated. There are multiple types of aberration, but we will limit the discussion to spherical aberration, which is typically the dominant aberration in a rotational symmetric geometry.

Spherical aberration causes asymmetry along the direction of propagation and is per definition caused by a radially dependent focal distance*. The optical field behind a rotational symmetric system with a positive lens with spherical aberration can be described using the following equation (see section 9.2).

$$E(\rho, z) = E_0 \int_0^{q_{\max}} q J_0(kq\rho) e^{-\left(\frac{q}{q_{\text{Gauss}}}\right)^2 - i\left(\pm\pi\left(\frac{q}{q_{\text{sphere}}}\right)^4 - kz\sqrt{1-q^2}\right)} \, dq \tag{3.2}$$

Where $q = \sin(\theta)$, $\rho$ and $z$ are the radial and transverse directions, $k$ the length of the wave vector, $q_{\max} = \sin(\theta_{\max})$ with $\theta_{\max}$ half the opening angle. $q_{\text{sphere}}$ and $q_{\text{Gauss}}$ have an equivalent definition, but they can be larger than 1. The $\pm$ corresponds to positive and negative spherical aberration respectively. $q_{\text{sphere}}$ describes the amount of spherical aberration and $q_{\text{Gauss}}$ describes the size of the input beam translated into terms of the opening angle behind the lens (it essentially describes how Gaussian the incoming light is). $J_0(x)$ is the zeroth order Bessel function of the first kind.

*In other words the focal distance changes radially from the centre to the edge of the lens.

## 3.3 Characterisation

### Parameters from literature

A Gaussian beam can be described with the following equation (See Svelto [14] and Mahajan [15] page 336):

$$I(\rho, z) = I_0 \frac{w_0}{w(z)} e^{-\frac{2\rho^2}{w(z)^2}} \tag{3.3}$$

and $w(z) = w_0\sqrt{1 + (z/z_R)^2}$.

A lens can be completely characterised by its effect on the phase front of incoming light, but it is really difficult to fully measure the phase front throughout space. This is why there are different parameters that try to capture aspects of the lens:

1. waist $w(z)$ and beam waist $w_0$
2. Rayleigh range $z_R$
3. Strehl ratio $S$

We can visualise the intensity distribution using an $I(\rho, z)$ plot. This is a false colour plot that shows the intensity distribution $I(\rho, z)$ along the direction of propagation ($z$) versus the transverse radial direction ($\rho$) (an example of an $I(\rho, z)$ plot is shown in figure 3.1). This allows one to visually inspect how the light propagates and see the effects of the phase front (through interference patterns). It is difficult to quantify the system through this method, so while a $I(\rho, z)$ plot visualises the situation we need to use other methods to characterise the system.

The *waist* $w(z)$ of a Gaussian beam can be found from (equation (3.3)) and is defined as:

$$I(w(z), z) = I(0, z)e^{-2} \tag{3.4}$$

We can define an equivalent waist for non-Gaussian distributions, although for extremely wild distributions there might be a need to define the waist as the largest waist. The waist is found in the same manner as the FWHM.

The *beam waist* $w_0$ is defined as the waist in the focus. For a diffraction limited Gaussian focus $w_0 = \lambda/\pi\text{NA}$ and for a diffraction limited Airy pattern

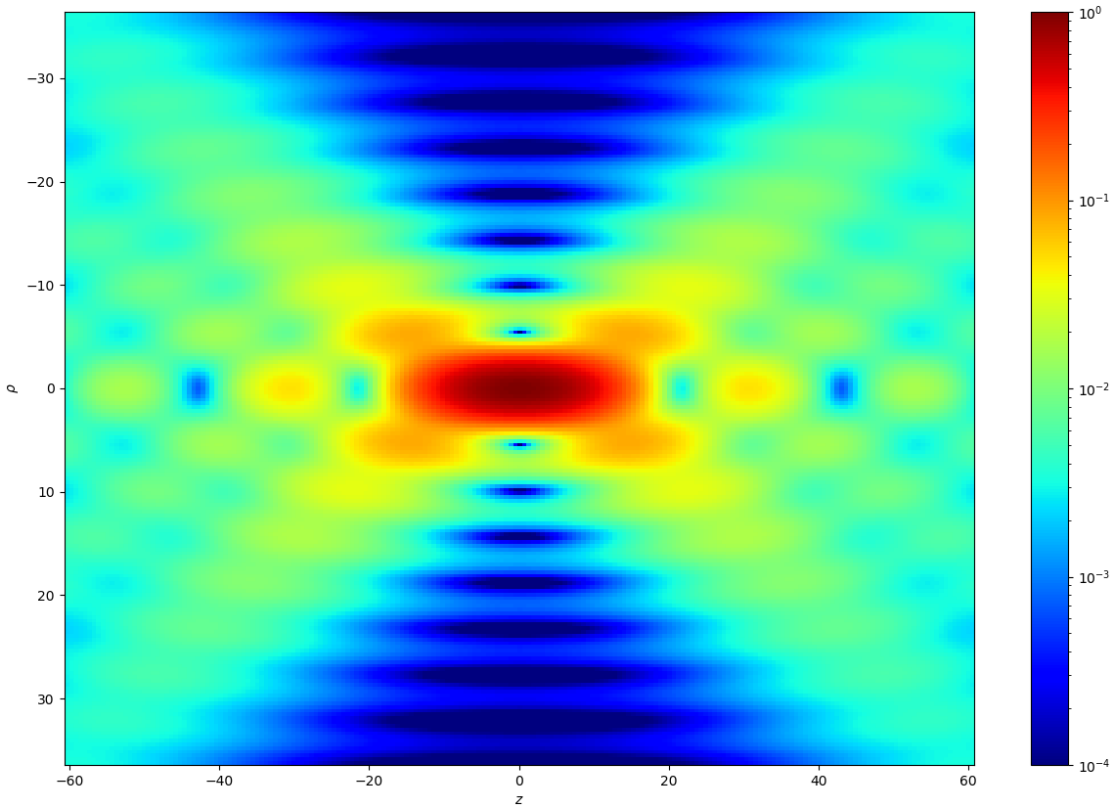


**Figure 3.1:** *A logarithmic false-colour $I(\rho, z)$ plot of an unaberrated focus of a fully illuminated positive lens, calculated using Equation* (3.2)*. The axes are in terms of the wave vector.*

$\Delta x = 0.61\lambda/\mathrm{NA}$ with $\Delta x$ the distance to the first zero in the Airy pattern.

The *Rayleigh range* $z_R$ is the distance from the focus such that the area of the cross-section doubles with respect to the focus. This definition is closely tied to the definition of the waist. For a Gaussian beam the following holds: $z_R = \frac{\pi w_0^2}{\lambda}$ and $\left(\frac{w(z)}{w_0}\right)^2 - \left(\frac{z}{z_R}\right)^2 = 1$.

The *Strehl ratio* $S$ is mathematically defined as (Mahajan [15] p. 54):

$$S = \frac{I_{aa}(0, z_i) z_i^2}{I_{uu}(0, z_g) z_g^2} \tag{3.5}$$

Where $I_{aa}(0, z_i)$ is the central intensity of the system at distance $z_i$ from the pupil. $I_{uu}$ is the central intensity of a diffraction limited system at distance $z_g$. $z_g$ is the Gaussian plane (the focus lies in this plane) and $z_i$ is the image plane.

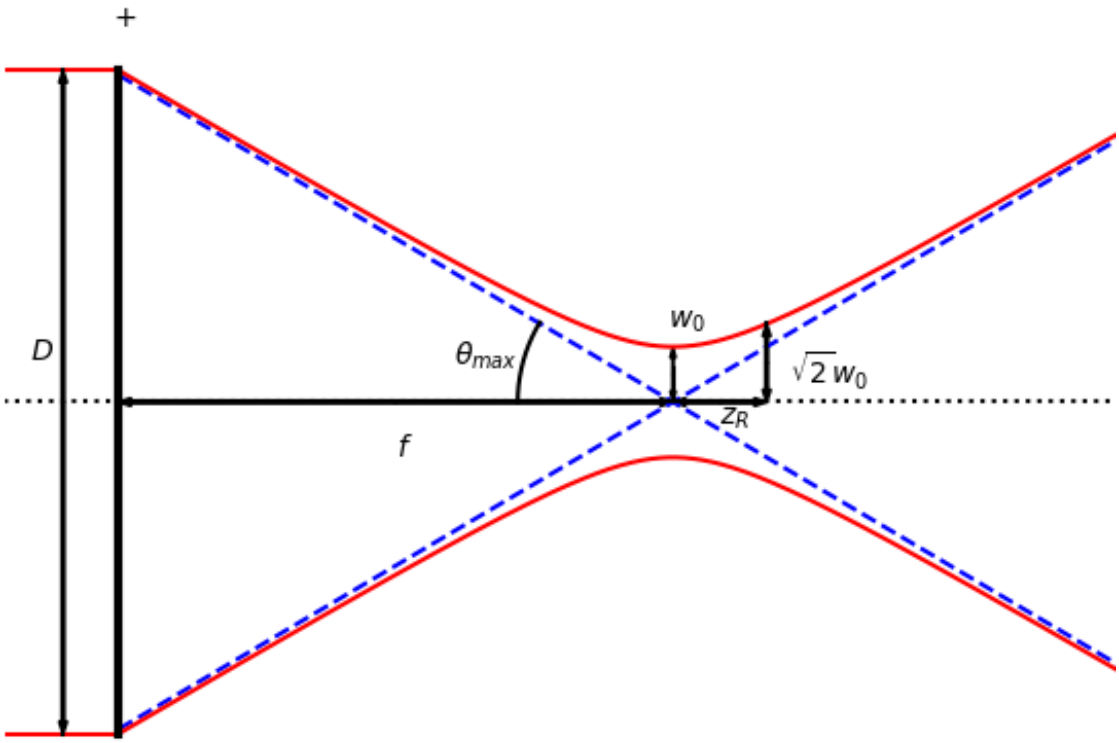


**Figure 3.2:** *An on-axis crossection of a Gaussian beam showing both the beam, lens and the following parameters: lens diameter $D$, working distance/focal length $f$, opening angle $f$, beam waist $w_0$ and the Rayleigh range $z_R$.*

If we use the peak value in the focus of the lens we have that $z_i = z_g$ and we can define.

$$S = \frac{I_{\text{peak}}}{I_{\text{peak, unaberrated}}} \tag{3.6}$$

where $I_{\text{peak}}$ is the peak intensity and $I_{\text{peak, unaberrated}}$ is the peak intensity if the system was unaberrated (for a perfect lens with a circular aperture the intensity profile is an Airy disk.).

Per definition it holds that $S \in [0, 1]$. The Strehl ratio can be difficult to compute, as it depends on how you illuminate your lens.

## Additional parameters

The following parameters can also be used to characterise a lens. We argue for their usefulness and define their role in the characterisation.

1. Transmissivity $T$

2. Focal Power Fraction $F$
3. Intensity amplification $\Omega$
4. z waist $\bar{z}$

We have chosen to define the focus to lie within the waist: Our focus reaches from the highest intensity to where the power is $e^{-2}$ of the highest intensity. For a radially symmetric 2d Gaussian distribution the fraction of the intensity that lies within the focus is roughly 86.5%, while for an Airy pattern this is roughly 77.1%[†].

The *transmissivity* is defined as the power in the focal plane within the lens radius $R$ divided by the power within that same radius if the lens was not there at all. It measure the amount of light actually passes through the lens.

$$T = \frac{P_{0,\text{with lens}}(R)}{P_{0,\text{without lens}}(R)} \tag{3.7}$$

The *focal power fraction* is defined as the power within the focus divided by the total power within a plane. We measure it by dividing the power in the focus by the power in a plane far away from the focus. It is a measure of the fraction of the power that is contained in the focus.

$$F = \frac{P_{z=0}(w_0)}{P_z(w \gg w(z))} \tag{3.8}$$

with

$$P_z(\rho) = \int_0^{\rho} \int_0^{2\pi} I(\rho', z)\, d\rho' d\theta \tag{3.9}$$

For a perfect Gaussian beam $F \approx 0.865$ and for a perfect Airy profile $F \approx 0.771$.

The *intensity amplification* is defined as the average intensity in the focus divided by the average intensity that hits the lens. We can also write this in terms of the focal power fraction, transmissivity and the relative change in area. It is a measure of how much light the lens manages to condense.

$$\Omega = \frac{\langle I_{\text{focus}} \rangle}{\langle I_{\text{in}} \rangle} \approx FT \frac{A_{|z|=f}}{A_0} = FT \left( \frac{D}{2w_0} \right)^2 \tag{3.10}$$

with

$$A_z = \pi w^2(z) \tag{3.11}$$

[†]See section 9.1



Version of June 18, 2019– Created June 18, 2019 - 14:17

For a diffraction limited Gaussian beam from a perfect lens we can write $\Omega$ as:

$$\Omega_{\text{Gauss, ideal}} \approx 0.865 \left( \frac{D\pi \text{NA}}{2\lambda} \right)^2 \tag{3.12}$$

The Strehl ratio can be approximated as

$$S = \frac{I_{\text{focus}}}{I_{\text{focus, ideal}}} \approx \frac{\langle I_{\text{focus}} \rangle}{\langle I_{\text{focus, ideal}} \rangle} = \frac{\Omega}{\Omega_{\text{ideal}}} \tag{3.13}$$

The $z$ *waist* $\bar{z}$ is the distance from the focal plane where the on axis intensity becomes $e^{-2}$. For a Gaussian beam we can use that the on-axis intensity distribution is $I(0,z) = I_0(1 + (z/z_R)^2)^{-1}$, so the z waist can be related to the Rayleigh range in the following way $\bar{z}^2 = z_R^2(e^2 - 1)$. The reason why this parameter is useful is because the density of data points is relatively low along the direction of propagation (in the setup used the density was one data point per 5 $\mu$m). Because the Rayleigh range is small (for a diffraction limited system the Rayleigh range is of the order of $\lambda$) the uncertainty on its measurement will completely dominate. For this reason the z waist, which is larger is be easier to determine.

The z waist, like the Rayleigh range, measures the length of the focus.

| Parameter | Character | Meaning |
|---|---|---|
| Numerical aperture | NA | $n \sin(\theta_{\text{max}})$ |
| Working distance | WD | Distance from the lens to the focus |
| Waist | $w(z)$ | $I(w(z), z) = I(0,z)e^{-2}$ |
| Beam waist | $w_0$ | $w_0 = w(0)$ |
| z waist | $\bar{z}$ | $I(0,\bar{z}) = I(0,0)e^{-2}$ |
| Transmissivity | $T$ | $T = P_{0,\text{with lens}}(R) / P_{0,\text{without lens}}(R)$ |
| Focal Power Fraction | $F$ | $F = P_0(w_0) / P_z(w \gg w(z))$ |
| Intensity Amplification | $\Omega$ | $\Omega = I_{\text{focus}} / I_{\text{in}}$ |
| Strehl Ratio | $S$ | $S = I(0,0) / I_{\text{diffraction limited}}(0,0)$ |

**Table 3.1:** *Summary of the parameters introduced in this chapter that we will be using to characterise foci. $z = 0$ is the on-axis focal position, $R$ is the lens radius, $A_z$ is the focal area at an on-axis position $z$, $P_z(w)$ is the power in a plane at position $z$ within radius $w$, and $\theta_{max}$ is the opening angle.*



Version of June 18, 2019– Created June 18, 2019 - 14:17

Chapter 4

# Micro-lens design, experimental setup and methods of characterisation

## 4.1 Designing and creating micro-lenses

There is a large number of different lenses that could be created using the Nanoscribe PPGT (see section 2.2 for more information), but two designs are exceptionally well understood: half ball lenses and thin lenses.

Both are also relatively easy to make and each has their own strengths and weaknesses. A half ball lens is a sphere cut in half. The light illuminates the curved surface and exits the length through the flat surface. The flat surface makes the lens easy to place on top of a structure, which has the added benefit of allowing the lens to work as a solid immersion lens. The big weakness of a half ball lens is that they introduce spherical aberration.

A half ball lens (see figure 4.1 for the design) with an infinite height illuminated by a parallel beam has the following focal length as a function of radial distance (see section 9.3):

$$\mathrm{f}(r) = R + \frac{\sqrt{R^2 - r^2}}{n^2 - 1}\left(1 + \sqrt{\frac{n^2R^2 - r^2}{R^2 - r^2}}\right) \tag{4.1}$$

with $R$ the radius of the lens and $n$ the refractive index.
In the paraxial limit this reduces to:

$$f \approx \frac{n}{n-1}R\left(1 - \frac{1}{2n^2}\frac{r^2}{R^2}\right) + \dots \tag{4.2}$$

A thin lens (see figure 4.2 for the design) is a lens with two curved surfaces. A perfect thin lens introduces no aberrations. A big weakness of a thin lens is

that the lens needs to be suspended above the structure somehow. This means that a structure needs to be designed to hold the lens and it is not unthinkable that this structure influences the light.

A thin lens obeys the lensmaker's equation (Mahajan [16] p.26):

$$\frac{1}{f} = (n-1)\left(\frac{1}{R_1} - \frac{1}{R_2}\right) \tag{4.3}$$

With $R_1$ and $R_2$ the radii of curvature. By using symmetric positive thin lenses ($R_c = R_1 = -R_2$) the lens obeys the following simple equation:

$$f = \frac{R_c/2}{n-1} \tag{4.4}$$

For a lens with $f = 40$ $\mu$m $R_c = 44$ $\mu$m and for f=100 $\mu$m $R_c = 110$ $\mu$m.

Because of these relations it is possible to calculate the expected optimal performance of designed thin and half ball lenses.

The lenses were designed in a program called Autodesk Inventor [17] and forwarded to J. Mesman-Vergeer of the Fine Mechanical Department. He operated the Nanoscribe Photonic Professional GT located on the tenth floor of the Huygens Laboratorium Leiden to print the lenses. These lenses were then analysed experimentally analysed.

## 4.2 Experimental Setup

The analysis of a lens is done by illuminating the lens and analysing the effects of the lens on the light beam. We do this by imaging the transmitted beam on a CCD camera and then using various techniques to analyse the various images taken.

The experimental setup is divided into three distinct parts: the light source; the lens to be analysed; and the imaging construction.

The light source was an alphaLAS Picosecond Pulse Diode Laser at 520 ($\pm$ 10) nm. The laser light was sent through four adjustable grey filters into a single mode AR coated fibre [18]. The end of the fibre was mounted behind a small lens (20X NA=0.40), by changing the distance between the lens and the fibre the spread of the resulting beam was changed. This beam is then used to illuminate a lens that we want to analyse. This lens creates a focus which was imaged on a CCD camera (Apogee Alta F1) using the combination of a 100X* lens and a f=20

*Nikon TU Plan Apo EPI 100X/0.9 OFN25 WD 2.0



Version of June 18, 2019– Created June 18, 2019 - 14:17

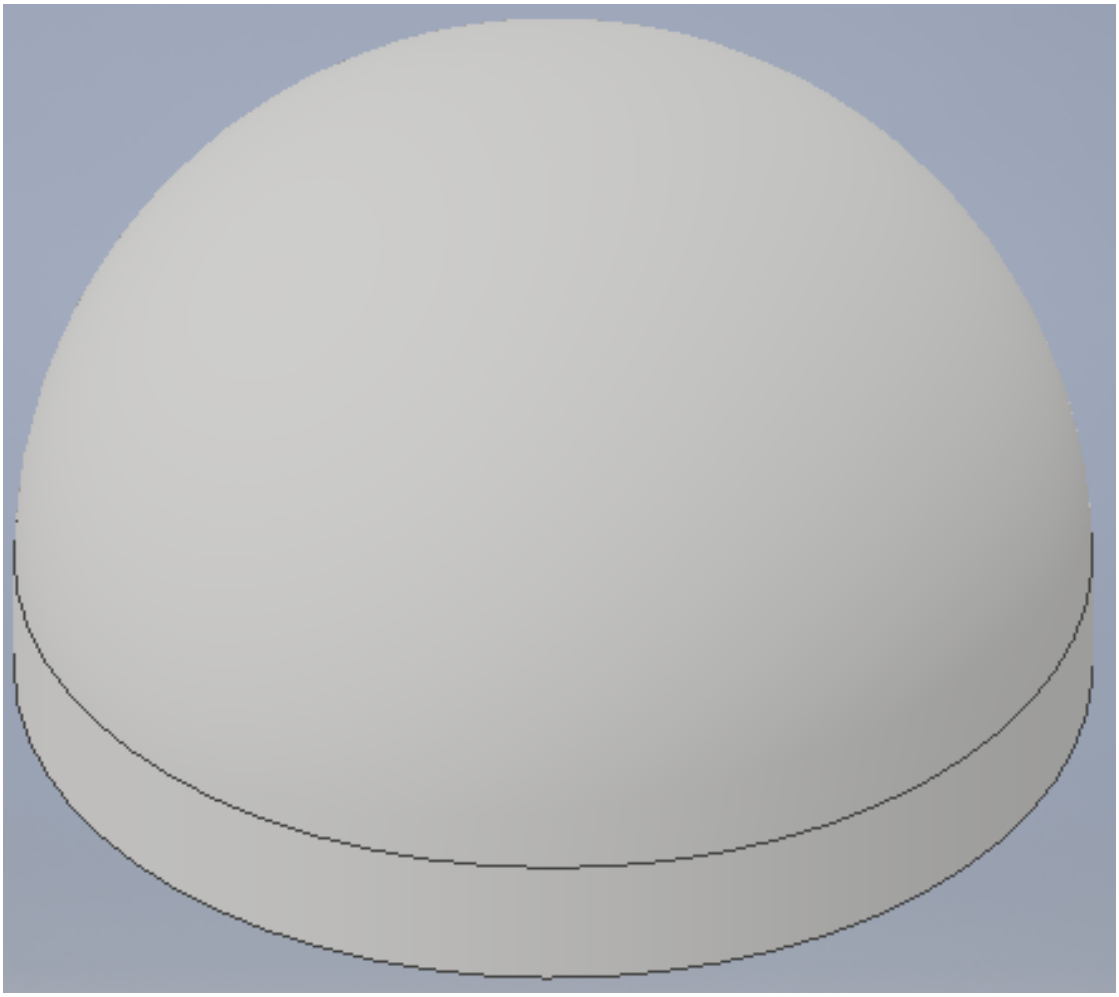

**Figure 4.1:** *Half Ball design. The design consists of two parts: half of a sphere with radius R; and a cylinder with radius R and height h.*

lens positioned at 20 cm behind the 100X lens. We also looked at the back focal plane of the 100X lens by changing the f=20 lens into an f=10 lens. This back focal plane image is used to estimate the transmission.

The 100X lens is mounted on a precision movable table, allowing the lens to move in all directions. We used this to not only align the image on the CCD camera, but also look at different positions along the direction of propagation. By imaging at intervals of $\Delta z = 5$ $\mu$m the entire 3d structure of the focus is imaged.

Four types of lenses will be analysed in this thesis. A close to perfect Mi-

tutoyo 20X objective[†]. A close to perfect Nikon 40X objective[‡]. 3D printed half ball and thin lenses printed using the Nanoscribe PPTG.

The near perfect lenses are as fully illuminated as possible (unless stated otherwise) by a slightly diverging beam. The 3d printed lenses are illuminated by a weak focus. The way of illumination can introduce (or compensate) spherical aberration. We expect that full illumination of an objective by a weakly diverging beam will not introduce spherical aberration (for more information see Stallinga [19]). The small lenses are illuminated by a weak focus, and as such the illumination can be treated to be near parallel.

A python program was written to load, reduce and analyse the CCD images that were made (see Github Repository [20]).

[†]Mitutoyo M Plan Apo NIR 20X/0.40 ∞/0 f=200
[‡]Nikon Plan Fluor ELWD 40X/0.60 ∞/0-2 WD 3.7-2.7 with correction ring



Version of June 18, 2019– Created June 18, 2019 - 14:17

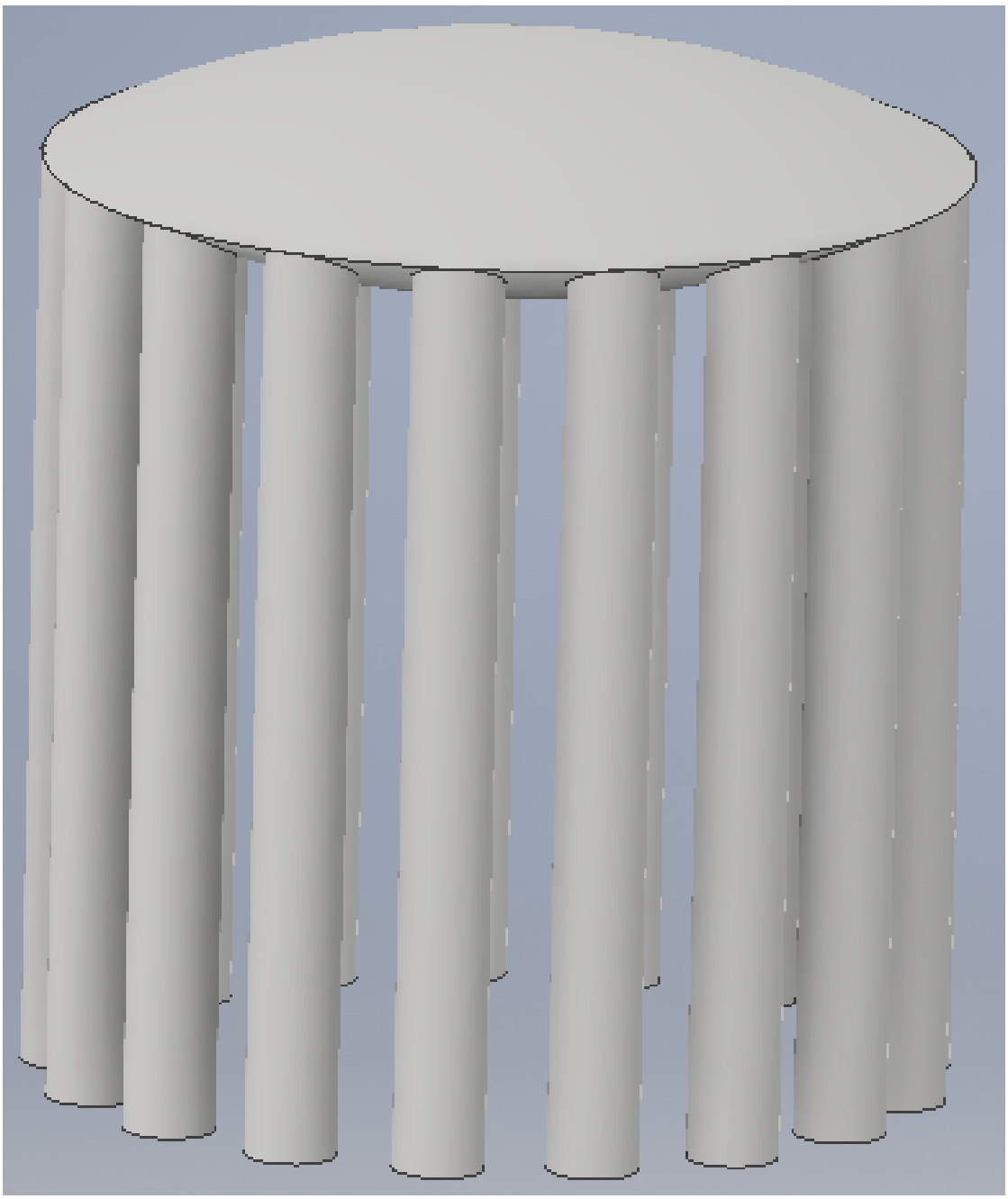

**Figure 4.2:** *Thin lens design. The design consists of two parts: a symmetrical thin lens designed to have diameter and focal length D; and 17 pillars that support the thin lens a distance D above the surface.*



Version of June 18, 2019– Created June 18, 2019 - 14:17

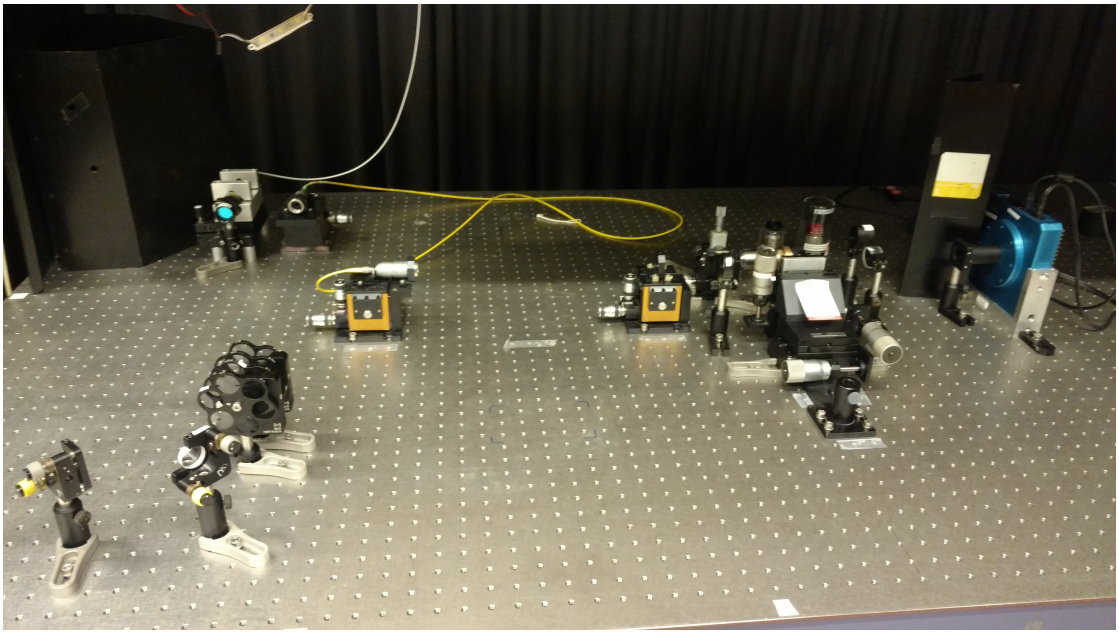

**Figure 4.3:** *The experimental setup. To the left is the laser and an alignment system aiming the laser at a fibre. To the right is the actual experiment.*

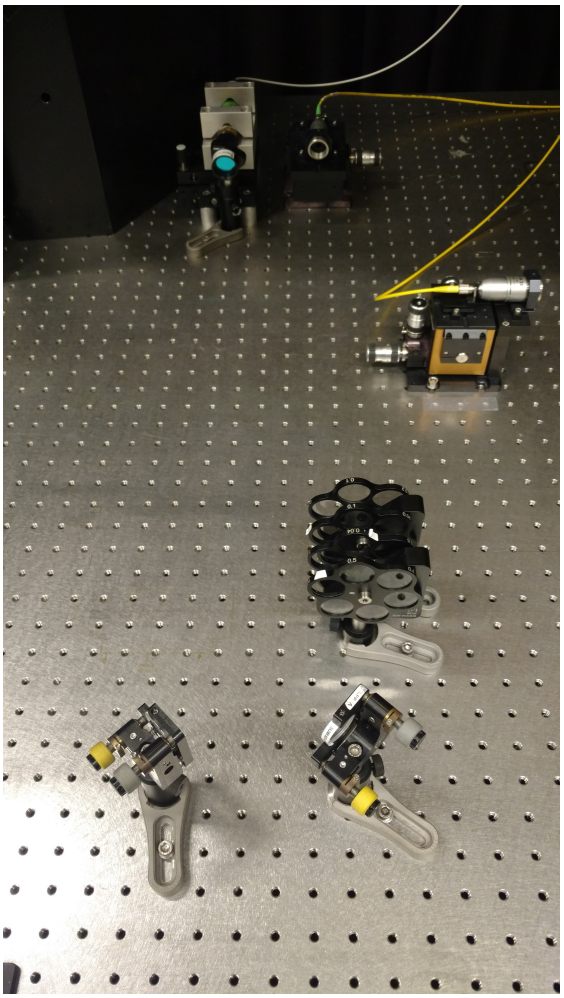

**Figure 4.4:** *The laser setup. On the top there is the laser (left) with a colour filter and a fibre entrance (right). Below there are the mirrors. Halfway on the right there are the grey filters (below half) and the fibre exit (above half).*

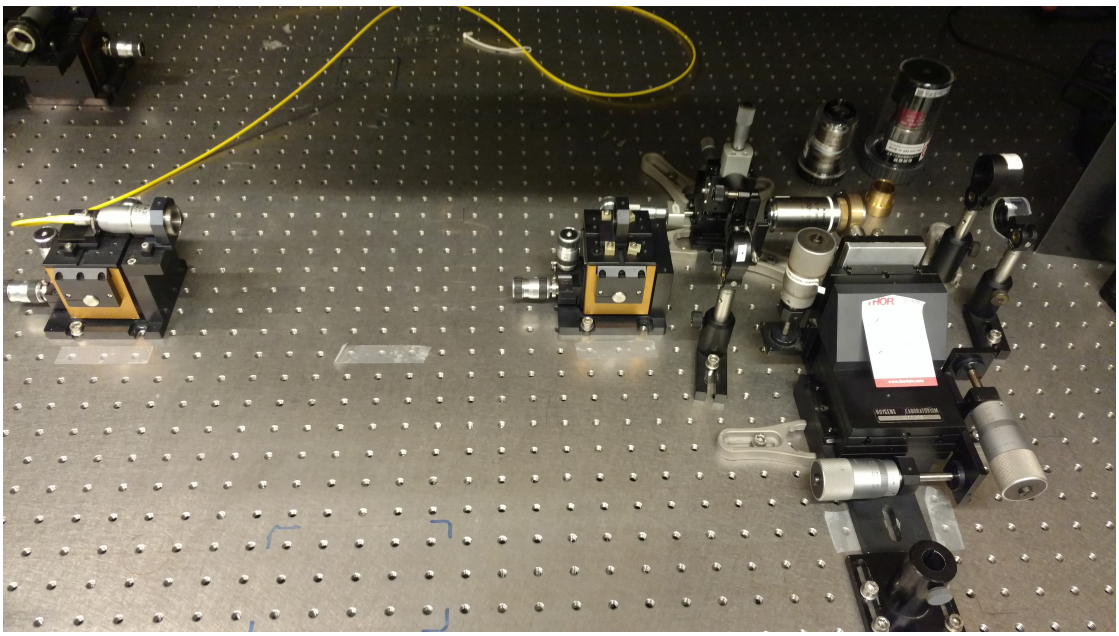

**Figure 4.5:** *The experimental setup, zoomed in. To the left is the fibre where laser light exits with a small lens to control the spread. In the middle there is a mount so that the 100X lens can scan in 3 dimensions, a small sample holder and a mount to hold objective lenses. To the right there are the imaging lenses.*

## 4.3 Fit procedure of a $I(\rho, z)$ plot

We begin with taking images at various positions around the focus along the direction of propagation. This allows us to image the entire 3d sturcture of the focus and by combining this data we can create an $I(\rho, z)$ plot. Figure 4.6 shows an $I(\rho, z)$ plot of one of the lenses we analysed (further characterised in section 5.3).

We can now use equation 3.2 to construct a $I(\rho, z)$ plot for a given amount of spherical aberration, pupil illumination and opening angle.

$$E(\rho, z) = E_0 \int_0^{q_{\max}} q J_0(kq\rho) e^{-\left(\frac{q}{q_{\text{Gauss}}}\right)^2 - i\left(\pm\pi\left(\frac{q}{q_{\text{sphere}}}\right)^4 - kz\sqrt{1-q^2}\right)} dq \tag{3.2}$$

We wrote a small python program that creates an image for given values of rho, z, $q_{\text{Gauss}}$, $q_{\text{sphere}}$, $q_{\text{open}}$. We can use this to try to fit figure 4.6 by eye. We will also discuss the advantages and disadvantages of this method.

We will try to fit figure 4.6 which we will also analyse later using the earlier discussed characterisation techniques.

Two fits have been made by eye, one created by the author and one by the supervisor M. P. van Exter. We knew that the opening angle of the system was 0.6, $q_{\text{sphere}}$ and $q_{\text{Gauss}}$ have been determined. The resulting best fits are shown in figure 4.7). We agree that $q_{\text{Gauss}} = 1$, but we disagree on $q_{\text{sphere}}$. Averaging the two $q_{\text{sphere}}$ found we get an estimate of $q_{\text{sphere}} = 0.27 \pm 0.02$. The error was estimated using difference in the parameters between the two fits.

While we can spot differences between figure 4.7, the coarseness of figure 4.6 is so high that we cannot find a better fit. This is the largest problem with this fit procedure: images with low resolution are difficult to fit. This method also needs multiple people to examine the image to ensure that the fit is accurate.

The advantage of this method is that it characterises the amount of spherical aberration in a quantitative parameter. This is especially important if you have an a priori estimate of $\theta_{\text{sphere}}$ which allows you to compare this with the measured $\theta_{\text{sphere}}$. It might also be possible to optimise a fit routine that can automatically produce a reasonable fit. This would make characterisation of spherical aberration much easier.

Due to the short amount of time we were not able to use this method to characterise the various focii discussed in this thesis. Future research could

attempt to use this method and compare their findings with literature.

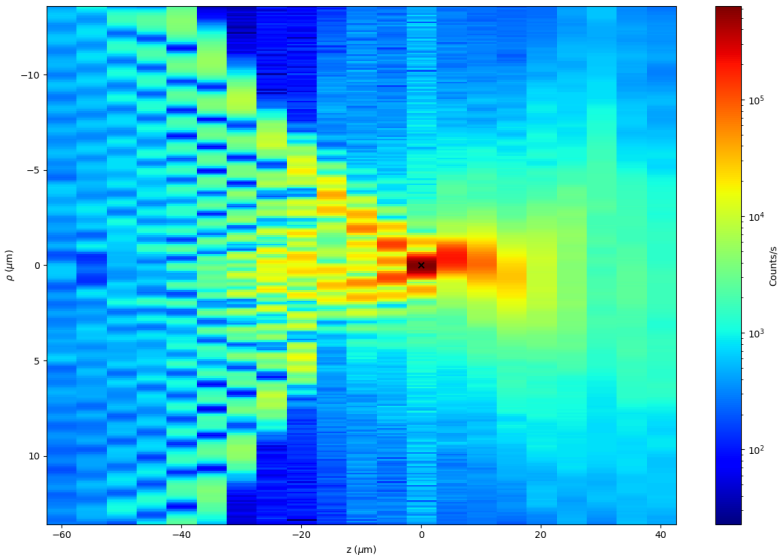


**Figure 4.6:** *A logarithmic false-colour plot of the intensity $I(\rho, z)$ measured behind a close to perfect perfect Nikon 40X lens, corrected for 0.4 mm cover glass. The lens is characterised in section 5.3*

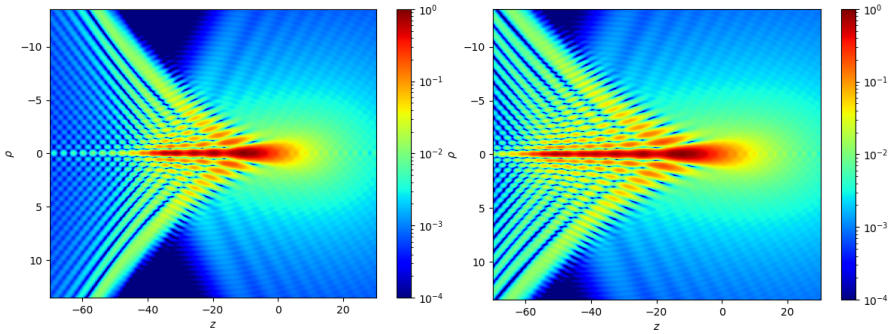


**Figure 4.7:** *Fits of figure 4.6 done by-eye. Left: found are $q_{sphere} = 0.29$ and $q_{Gauss} = 1$. Right: found are $q_{sphere} = 0.26$ and $q_{Gauss} = 1$.*

Chapter 5

# Characterisation of near perfect microscope objectives

## 5.1 Mitutoyo 20X objective

We begin with characterising the Mitutoyo 20X objective [21] which is as fully illuminated as possible. This is done using a slightly diverging beam (the distance between the fibre and lens is 38 cm, the diameter of the beam measured as 2 cm). This divergence can influence the working distance and NA.

After collecting images of the beam at different positions around the focus along the direction of propagation, the characterisation begins with looking at a visualisation of the beam through a $I(\rho, z)$ plot (figure 5.1). We see that the system is almost completely rotational symmetric and as such we will not show the variation along the y-axis from now on. We also observe that there is a slight asymmetry along the direction of propagation. This asymmetry suggests that the system has some internal spherical aberration.

Figures 5.2 to 5.4 show some individual CCD images and the intensity distribution along a horizontal and vertical axis at three different z-positions. The intensity distributions has been fitted with a Gaussian fit in each of the images.

Figure 5.3 shows the image nearest to the focus plane. Visible is the first Airy ring and the central disk. The peak of the first Airy ring is at approximately 3.2% of the peak intensity. The theoretical value for the Airy pattern is 1.7%. The discrepancy is probably caused by spherical aberration.
The Gaussian fit ($\gamma(r, \sigma) = Ae^{-(r^2)/(2\sigma^2)}$) of the intensity distribution gives a good fit of the central disk. We could use the standard deviation as an estimate to the beam waist. When $x = 2\sigma$ the Gaussian distribution gives $\gamma(2\sigma, \sigma) = Ae^{-(4\sigma^2)/(2\sigma^2)} = Ae^{-2}$, which means that the beam waist and the standard devi-

ation of a Gaussian fit are related in the following way: $w_0 = 2\sigma$. The estimate of the beam waist from the standard deviation of the Gaussian fit is then 0.67 ($\pm$ 0.05) $\mu$m. We can also find the beam waist using the definition as given in section 3.3. Using this method the waist was measured to be 0.65 ($\pm$0.05) $\mu$m (We estimate the error from the distance between two pixels on the CCD camera). The Gaussian fit seems to also be a valid method of estimating the beam waist.

By drawing a straight line between two data points we estimated the value of the waist (and z waist) between two data points. This gives a more accurate estimate of the value, but does not reduce the error.

From the image it is also possible to estimate the distance from the central maximum to the first zero of the airy disk, which is 1.0 ($\pm$0.1) $\mu$m. For a diffraction limited beam the expected distance is $\Delta x = 0.61\lambda/\mathrm{NA} = 0.79$ $\mu$m. This shows that the focus is close to, but not at, the diffraction limit (off by 26%). We hypothesise that the spherical aberration in the system is the reason why the diffraction limit is not reached.

The z waist is found to be $\bar{z} = 9$ ($\pm$2.5) $\mu$m (we estimate the error from the z-distance between two CCD images). The Rayleigh range can be calculated from the z waist for a Gaussian beam using the following equation: $z_R = \bar{z}/\sqrt{e^2 - 1}$. For a Gaussian beam this would give a Rayleigh range of 3.6 ($\pm$ 1) $\mu$m. From the specifications [21] we learn that the indicated depth of focus is 1.7 $\mu$m. That means that the indicated Rayleigh range is 0.85 $\mu$m. The difference is probably because there is spherical aberration in the system.

Looking at figures 5.2 and 5.4 one thing is very clear: there is a large difference between the two. Figure 5.2 has an intensity distribution that looks a lot like a top hat and estimating the waist is very easy. Just looking at the intensity distribution we estimate the waist to be roughly 9 $\mu$m, which in the CCD image is roughly the radius to where the intensity is 1/10 of the peak intensity.

Figure 5.4 has an intensity distribution that looks far more Gaussian. Estimating the waist is difficult and one could easily measure the waist to be 5 $\mu$m using the previous criterion of 1/10 of the peak intensity. It is easy to underestimate the waist in this regime, using the criterion of 1/100 of the peak intensity does seem to give roughly the same waist as before.

In both cases the Gaussian fit does not reflect the situation accurately anymore. We have also seen that it is very easy to under estimate the waist of the beam and that the criterion for estimating the waist lies much lower than one would expect (in comparison to the half width at half maximum and half width $e^{-2}$ of the maximum).

A parameter that, at first glance, can easily be estimated from Figure 5.1 is the Numerical Aperture. At the left side a rough estimation would be that the opening angle, indicated by the red line, is 0.34 ($\pm$0.05) (we estimate the error by using multiple reasonable estimates for the opening angle) giving an NA $\approx$ 0.34 ($\pm$0.05) which differs by 20% from the specified value of 0.4. We expect that the diverging beam used to illuminate the lens is the reason for the slight offset in NA. We would argue that this method, while being rough, gives a somewhat reasonable estimate of the Numerical Aperture.

We could estimate the working distance from the pupil diameter and the NA. We can estimate the WD using the following equation WD $= D/2$NA (see 3.1). The pupil diameter of the lens was measured to be 2.00 ($\pm$0.02) cm, giving a WD $\approx$ 2.9($\pm$0.4) cm. The specified working distance is 20 mm, which is almost 15 times smaller. We don't understand why the difference is so large and the only explanations that come to mind are: The lens is not fully used and as such the effective diameter is much smaller; Compound lenses are intricate and equation 3.1 simply does not hold in those cases. It is interesting to find out what the reason is, but this goes beyond the scope of this thesis.

The focal power fraction is defined in section 3.3. To find it we first calculate the power in the focus. Then we calculate the total power captured by the CCD camera in every plane. Finally we divide the power in the focus by the various total powers which creates a list of focal power fractions. We average of the focal power fraction calculated for the various planes (and use the standard deviation of the list as an estimate of the error). In figure 5.1 we notice that the focal plane has a high background, we tried isolating the system but we could not get rid of this background. Prof. C. U. Keller has suggested that the high intensity can cause the bias to rise, which would explain this phenomenon. We manually subtract this background in the focal plane when we calculate the focal power fraction (and intensity amplification).

We find that $F = 0.77$ ($\pm$ 0.11). For a diffraction limited beam this would be 0.771 (see section 9.1), so from the focal power fraction we would estimate that the beam is diffraction limited. We could not measure the intensity at the entrance pupil, so we make use of the following relationship: $\Omega \approx FTA_{z=f}/A_0$. For these near perfect lenses it is reasonable to assume that the transmissivity is 1. This gives $\Omega = 1.79 \cdot 10^8$ ($\pm 4.5 \cdot 10^6$).

From the focal power fraction we learn that 77% of the light that passes through the lens is actually condensed into the focus. From the intensity amplification we learn that the average intensity in the focus is roughly 180 million



Version of June 18, 2019– Created June 18, 2019 - 14:17

times larger than the average intensity if the lens was not there. This estimation is based on the measured lens diameter and if the full lens is not used the real intensity amplification is lower.

We can approximate the Strehl ratio as:

$$S \approx \frac{\Omega}{\Omega_{\text{ideal}}} = \frac{FT}{F_{\text{ideal}}} \frac{A_{0,\text{ideal}}}{A_0} \tag{5.1}$$

Because the focal power fraction is equal to the diffraction limited focal power fraction and we estimated that the transmissivity is 1 we get that $S \approx (w_{0,\text{ideal}}/w_0)^2$. For a diffraction limited focus the distance from the central maximum to the first zero in the Airy distribution for an NA = 0.4 is $\Delta x = 0.793$. Using this we have that $S \approx (0.793/1)^2 = 0.63$ ($\pm 0.06$). The Strehl ratio gives an estimation of the amount of aberration in the system.

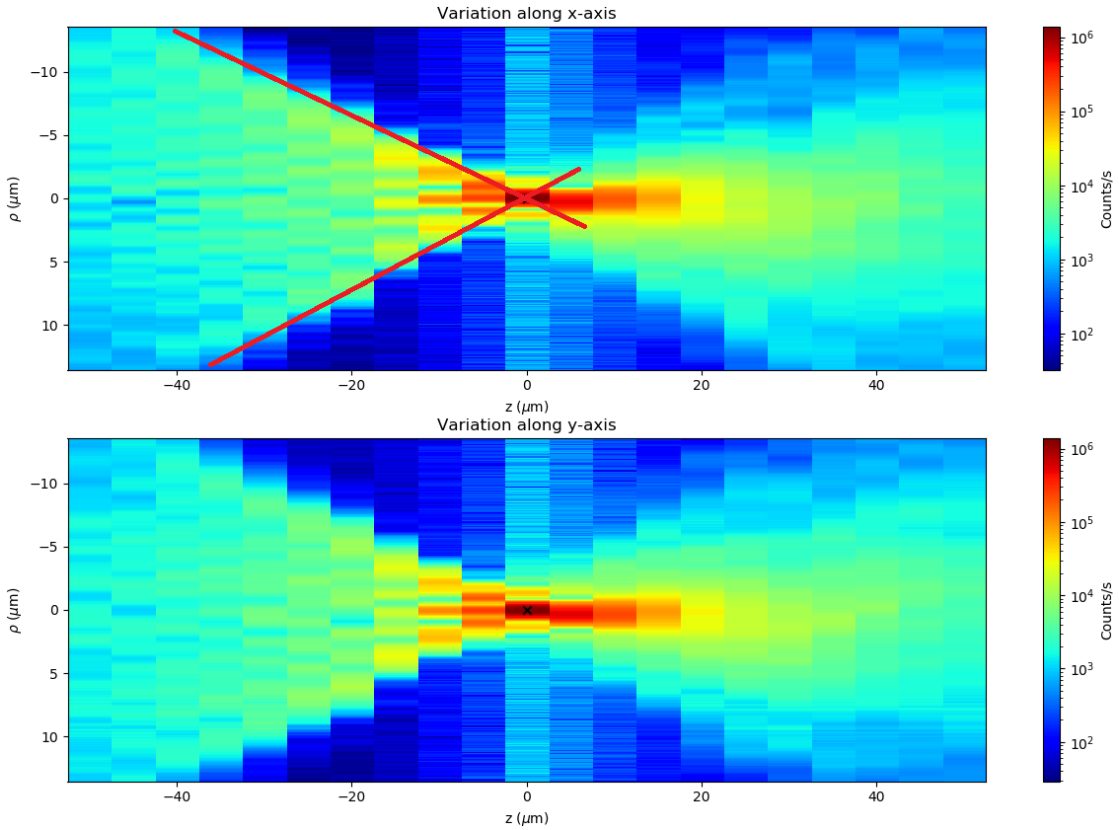


**Figure 5.1:** *A logarithmic false-colour plot of the intensity $I(\rho, z)$ measured behind a close to perfect Mitatoyu 20X lens. Both axes are in units of μm. The top plot has $\rho$ vary along the x-axis of the CCD camera, the bottom along the y-axis. Note: even in this figure we observe spherical aberration.*

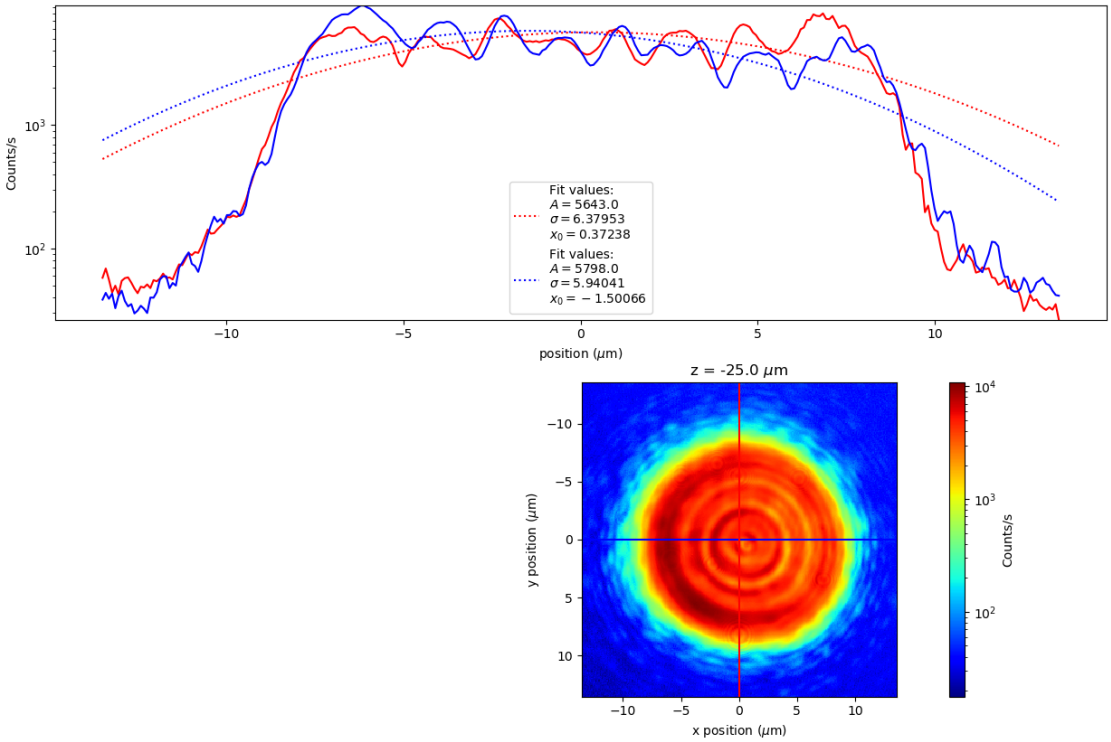


**Figure 5.2:** *A cross section of the intensity along the x and y direction (top figure). A logarithmic false-colour plot of the intensity $I(x, y)$ measured behind a close to perfect Mitutoyo 20X lens (bottom figure). Both at relative position $z = -25$ μm.*

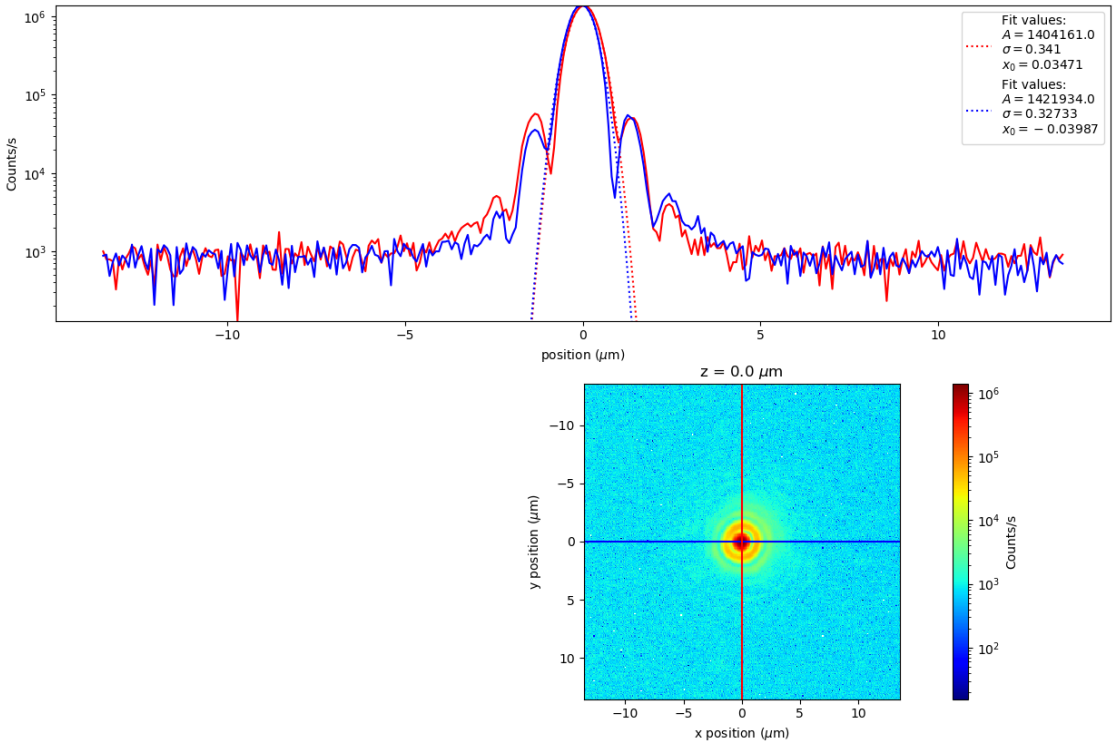


**Figure 5.3:** *A cross section of the intensity along the x and y direction (top figure). A logarithmic false-colour plot of the intensity $I(x,y)$ measured behind a close to perfect Mitutoyo 20X lens (bottom figure). Both in the focal plane ($z = 0$ $\mu m$).*

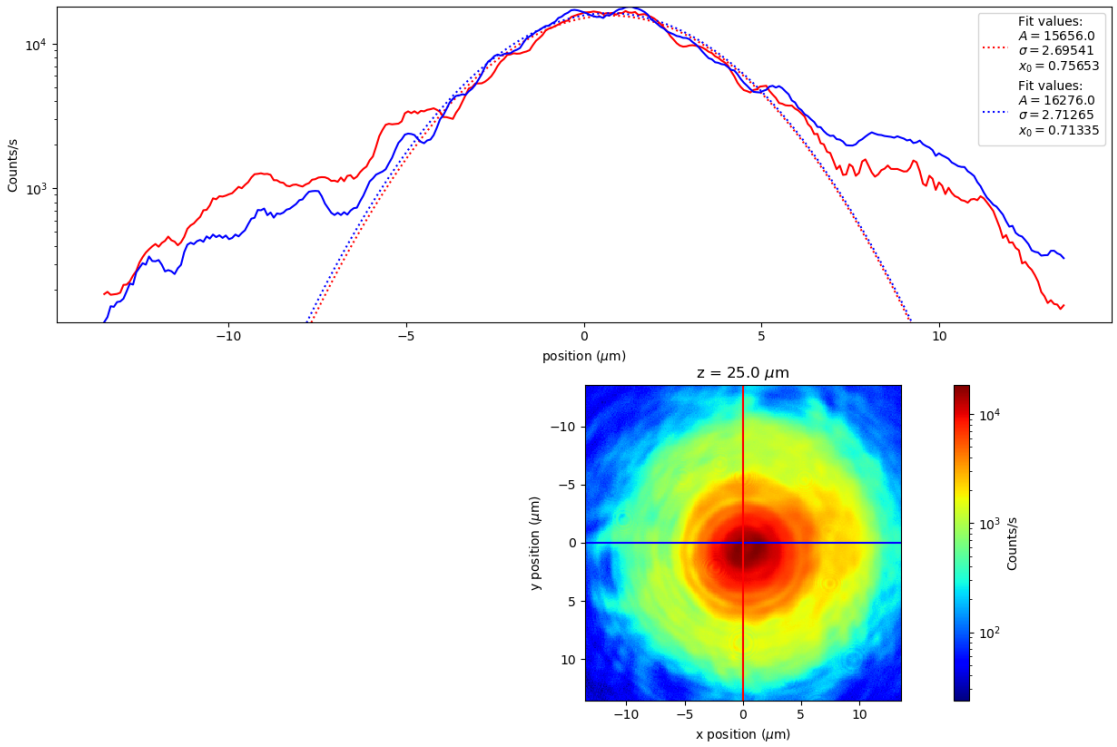


**Figure 5.4:** *A cross section of the intensity along the x and y direction (top figure). A logarithmic false-colour plot of the intensity $I(x, y)$ measured behind a close to perfect Mitutoyo 20X lens (bottom figure). Both at relative position $z = 25$ μm.*

We also considered the situation where the lens is not fully illuminated (figure 5.5).

Using the indicated red lines in this figure the NA of the Gaussian beam changes to 0.26 $\pm$0.05. The NA has changed because the beam diameter changed which in turn changed $\theta_{max}$. Under the assumption that we would still measure the same focal length using the same technique, we can now extrapolate the beam diameter. WD $\approx$ 2.9 ($\pm$0.2) cm gives $D \approx$ 1.7 ($\pm$0.05) cm, meaning that the pupil entrance was 72% illuminated. We were trying to get around 50% illumination (by eye).

The intensity profiles shown in figures 5.6 and 5.8 show two things: First, the beam has become slightly more symmetric, but the figures still differ. We also see that the Gaussian fits seem to describe the shape somewhat better than before. Figure 5.7 shows that the focus has become wider and more Gaussian, the first Airy ring is barely present (peak of the first ring at approximately at 0.5% of the peak intensity).

The beam waist is found to be 0.85 ($\pm$0.05) $\mu$m. We estimate the diffraction limited focus for a Gaussian beam (because the first Airy ring is just visible in log scale). $w_{diff} = \lambda / \pi \mathrm{NA} = 0.64$ ($\pm$0.12) $\mu$m. The measured waist is 33% larger than the diffraction limited waist. It is surprising that the focus is further away from the diffraction limit than before. We hypothesise that this is because of spherical aberration in the system which affects the edge of the beam more than the centre. The full illumination used before cuts off the edge of the beam, thus reducing the aberration. This might be interesting to explore further at another time.

The z waist is again found to be 9 ($\pm$2.5) $\mu$m. The resulting Rayleigh range is thus 3.6 $\pm$1 $\mu$m. The reason that this is much larger than the indicated Rayleigh range of 0.85 $\mu$m (see Mitutoyo [21]) is probably spherical aberration. Interestingly enough the Rayleigh range has not changed between the full and partial illumination. Because the waist is further from the diffraction limit we would expect that the Rayleigh range also increases.

The focal power fraction is calculated to be a surprising 1.14 ($\pm$0.18). This is a surprising result, for it would mean that there is more light passing through the focus than through the beam far away from the focus. This makes no sense from ray optics (it should be physically impossible for $F > 1$) and we don't know what is happening. An explanation would be that at large values of $z$ parts of the beam fall outside of the CCD image and are thus not taken into ac-

count. Calculating the focal power fraction by hand (and estimating the waist by eye) gives an estimation of $F = 0.8 \pm 0.2$, which makes more sense.
Using this focal power fraction and the beam diameter we calculated the intensity amplification to be $\Omega = 3.2 \cdot 10^8$ $(\pm 9 \cdot 10^7)$.
The diffraction limited focus has a beam waist of $w_0 = 0.64$ $\mu$m. From this we can estimate the Strehl ratio as $S = 0.54 \pm 0.15$. The Strehl ratio for this situation and the fully illuminated situation measured to be the same (they lie within each others error interval). As such we cannot draw the conclusion that there is more spherical aberration in the system.

In the previous sections we noticed that:

The fits to the intensity distributions can be used for characterising the intensity distribution of the focus. The Gaussian fits do not contribute additional information to our characterisation of the lenses. From now on we will not show these fits anymore. Around the focus a Gaussian fit could be used effectively, but far away from the focal plane a Gaussian distribution is not a good fit for an aberrated system.

A good estimate for the Numerical Aperture can be found for an unaberrated focus using a $I(\rho, z)$ plot.

For fully illuminated near perfect 20X Mitutoyo lens, the distance from the central maximum to the first zero in the bessel function is 26% larger than the diffraction limit. For the partially illuminated case this is 33%. We hypothesise that the reason why the system is not fully diffraction limited is aberrations in other parts of the setup. This claim seems to be supported by the fact that there is spherical aberration visible.

The transmission has not been calculated, but it is reasonable to assume that it is near 1 for the near perfect lenses.

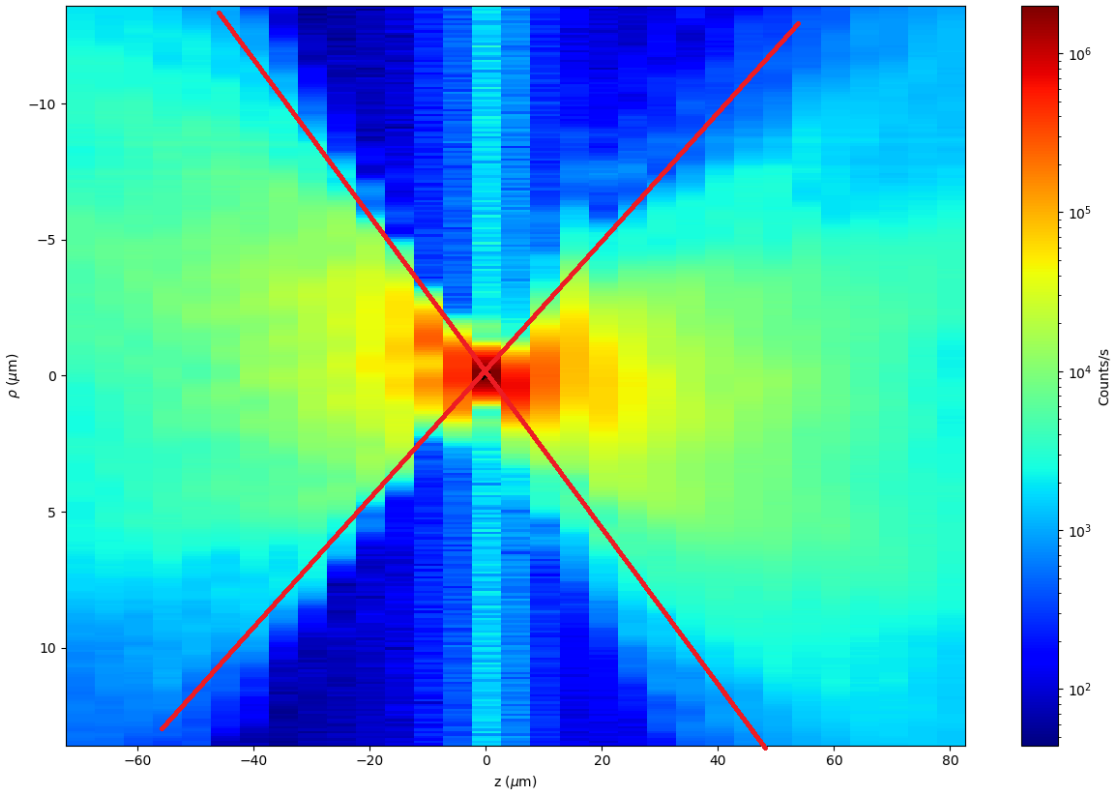


**Figure 5.5:** *A logarithmic false-colour plot of the intensity $I(\rho, z)$ measured behind a close to perfect Mitatoyu 20X lens which is not fully illuminated.*

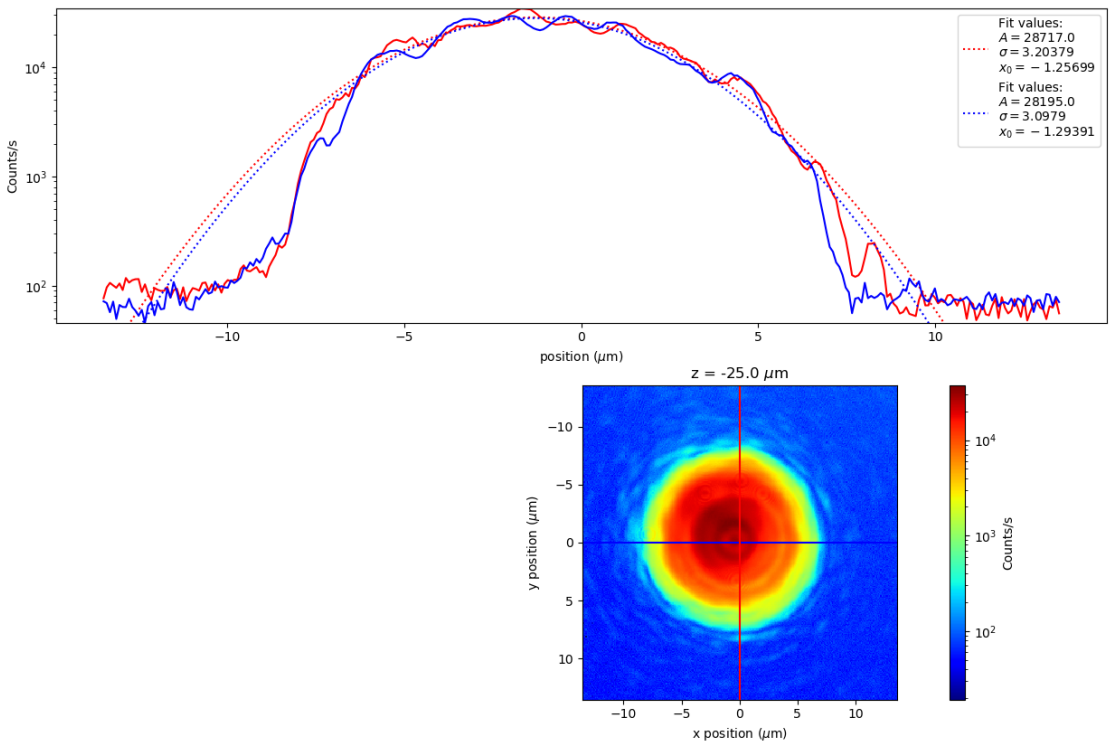


**Figure 5.6:** *A cross section of the intensity along the x and y direction (top figure). A logarithmic false-colour plot of the intensity $I(x, y)$ measured behind a close to perfect Mitutoyo 20X lens (bottom figure). Both at relative position $z = -25$ μm.*

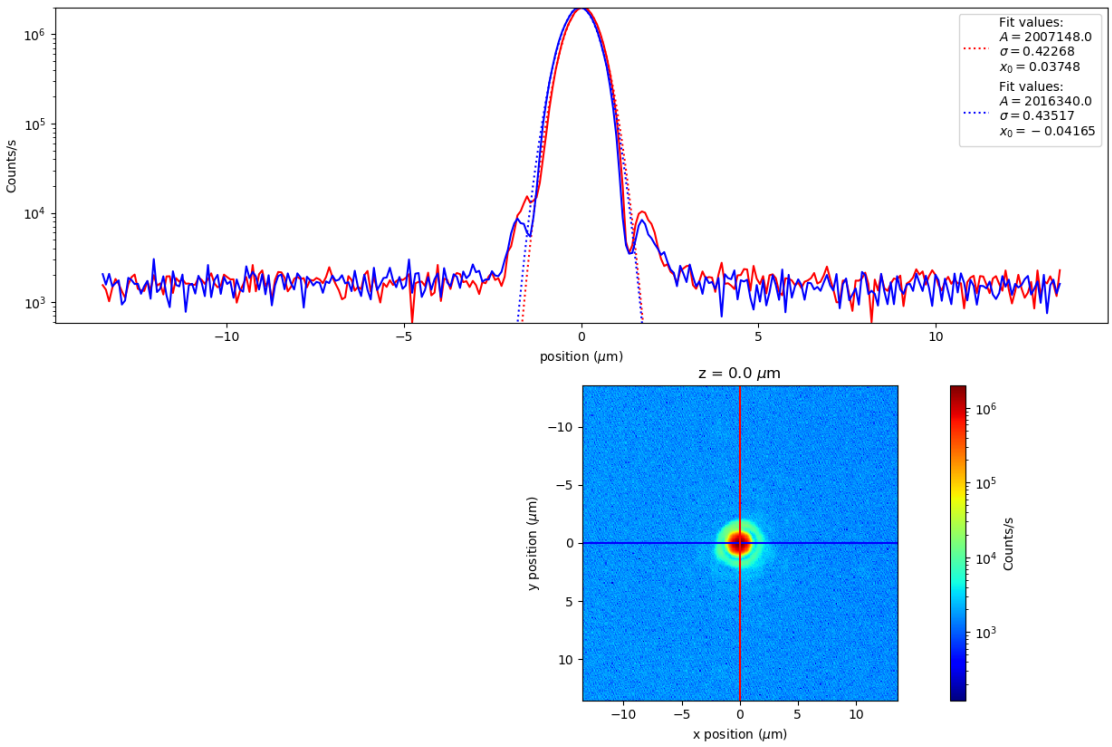


**Figure 5.7:** *A cross section of the intensity along the x and y direction (top figure). A logarithmic false-colour plot of the intensity $I(x, y)$ measured behind a close to perfect Mitutoyo 20X lens (bottom figure). Both in the focal plane ($z = 0$ μm).*

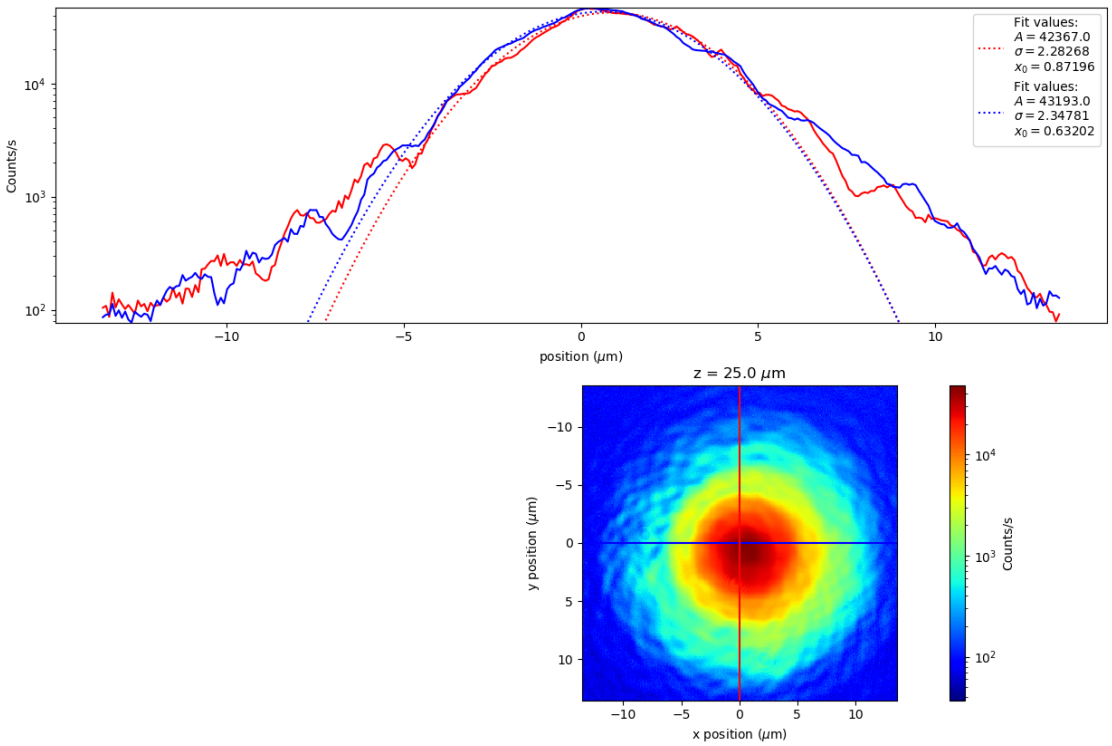


**Figure 5.8:** *A cross section of the intensity along the x and y direction (top figure). A logarithmic false-colour plot of the intensity $I(x, y)$ measured behind a close to perfect Mitutoyo 20X lens (bottom figure). Both at relative position $z = 25$ μm.*

## 5.2 Mitutoyo 20X objective with a parallel plate of thickness 6 mm

Spherical aberration can be introduced into the system by placing a parallel plate in the path of the focus. The parallel plate used is a fused silica parallel plate of thickness 6 mm. It becomes clear why this introduces spherical aberration if we look at the following equation for the change in focal length that a parallel plate introduces(see section 9.4):

$$\Delta f = d\left(1 - \frac{\cos(\theta)}{\sqrt{n^2 - \sin^2(\theta)}}\right) \tag{5.2}$$

with $d$ the thickness, $\theta$ the angle of incidence and $n$ the refractive index.
In the paraxial limit we can taylor expand this and see that:

$$\Delta f \approx d\left(\frac{n-1}{n} + \frac{n^2-1}{2n^3}\theta^2 + \dots\right) \tag{5.3}$$

In this form it is obvious how the plate changes the focus. The focus is shifted proportional to the thickness and refractive index ($\Delta f_0 = d(n-1)/n$). What is also visible is that there is a relative shift from the new focus which is also proportional to the angle of incidence $\Delta f_1 = \theta^2 d(n^2-1)/2n^3$. The only observed change to a $I(\rho, z)$ plot is the second term, which changes the light depending on the angle of the light ray (and thus for a non-parallel beam the radial position).

In figure 5.9 the spherical aberration is more visible than we have seen before. On the negative side of the $z$ axis the focus looks roughly like a Gaussian beam, but on the positive side there are numerous "fringes". Figures 5.10 to 5.12 show how individual images are affected. To the negative side of the focus we see the so called "powder box", the intensity distribution looks almost Gaussian. In the focus we see patterns resembling Airy rings surrounded by a lot of structure. To the right we see the so called "bulls-eye" which has a lot of ring structures. According to convention we call this configuration negative spherical aberration (half ball lenses introduce positive spherical aberration).

In total it is obvious that the beam is non-symmetric around its focus.

Trying to measure the NA appears to fail spectacularly (see figure 5.9). On the side of the powder box our estimate (using the black lines in figure 5.9) for the NA is roughly 0.11 ($\pm$0.05). On the side of the bulls-eye our estimate (using the red lines in figure 5.9) increase to 0.14 ($\pm$0.05), which is still nowhere close to our original (unaberrated) estimate of 0.34.

The reason for the mentioned discrepancy becomes clearer when the reason for the ring structures is taken into account. The ring structures are probably interference patterns and not the edge of the beam. We can also understand this from a ray optics view: spherical aberration is caused because the outer light rays are refracted less than the inner light rays. This will cause these rays to cross paths, creating rings where the rays overlap. More research is needed to confirm this theory.

The question that now arises is whether we can use the measured NA to say something about how much spherical aberration there is in the system? We will return to this in section 5.3.

We estimate the distance to the first zero in the Airy pattern to be 1.5 ($\pm$0.1) $\mu$m (a 50% increase from before) and the z waist to be 30 ($\pm$ 2.5) $\mu$m. Spherical aberration is directly responsible for this huge increase. We expected the increase in the beam waist, but the large increase to the z waist was surprising. This means that an aberrated beam is more extended along the direction of propagation. Spherical aberration increases the Rayleigh range of a beam.

The focal power fraction is estimated to be 0.45 ($\pm$0.07). This is a lot lower than before, which makes sense. Spherical aberration causes non-paraxial rays to be outside the focus.

The intensity amplification is then $3.7 \cdot 10^7$ ($\pm 7 \cdot 10^6$), about 21% of what we had before. The spherical aberration messes up the path of the light rays, thus reducing the focal power fraction and intensity amplification.
We can again find the Strehl ratio if we use the indicated NA (0.4) and the diffraction limited distance to the first zero in the Airy pattern ($\Delta x = 0.61\lambda \text{NA}$). This gives an estimate of

$$S \approx \frac{0.45}{0.771}\left(\frac{0.79}{1.5}\right)^2 \approx 0.163 \pm 0.03 \tag{5.4}$$

The Strehl ratio is a lot smaller than before (without plate $S = 0.63 \pm 0.06$). The Strehl ratio indicates that the system has become more aberrated, which is exactly what we expected.



Version of June 18, 2019– Created June 18, 2019 - 14:17

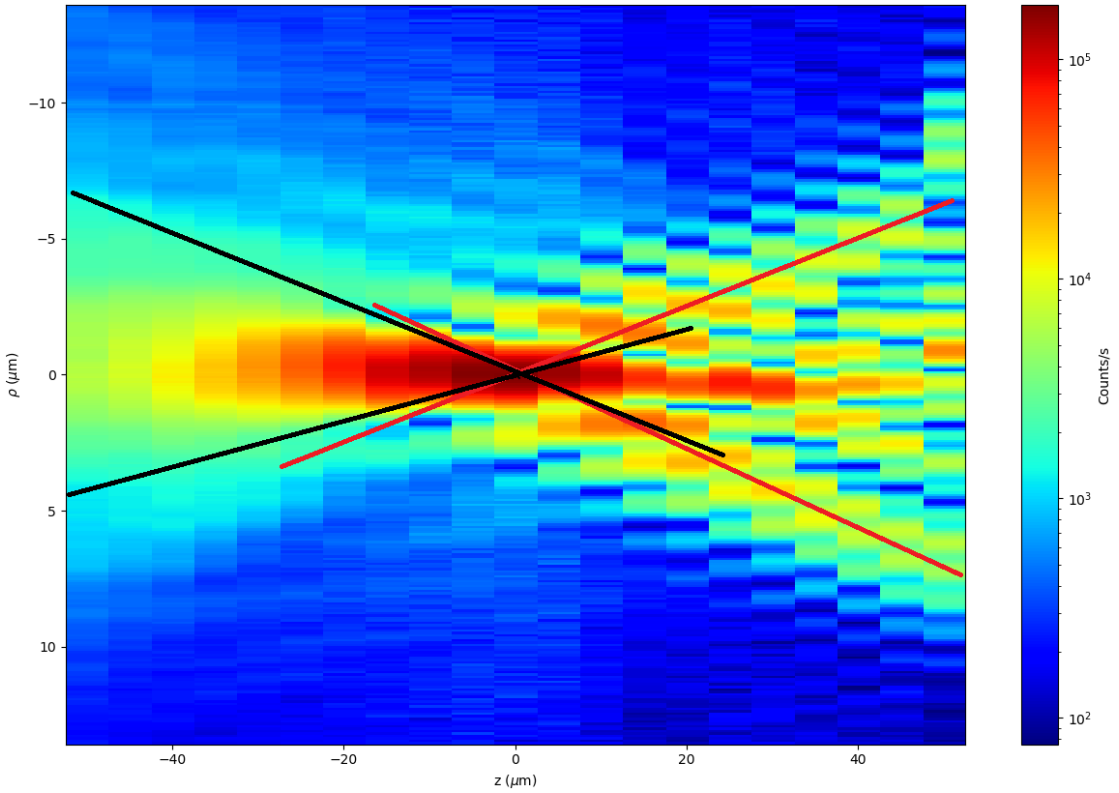


**Figure 5.9:** *A logarithmic false-colour plot of the intensity $I(\rho, z)$ measured behind a close to perfect Mitutoyo 20X lens, with spherical aberration introduced by 6mm of glass.*

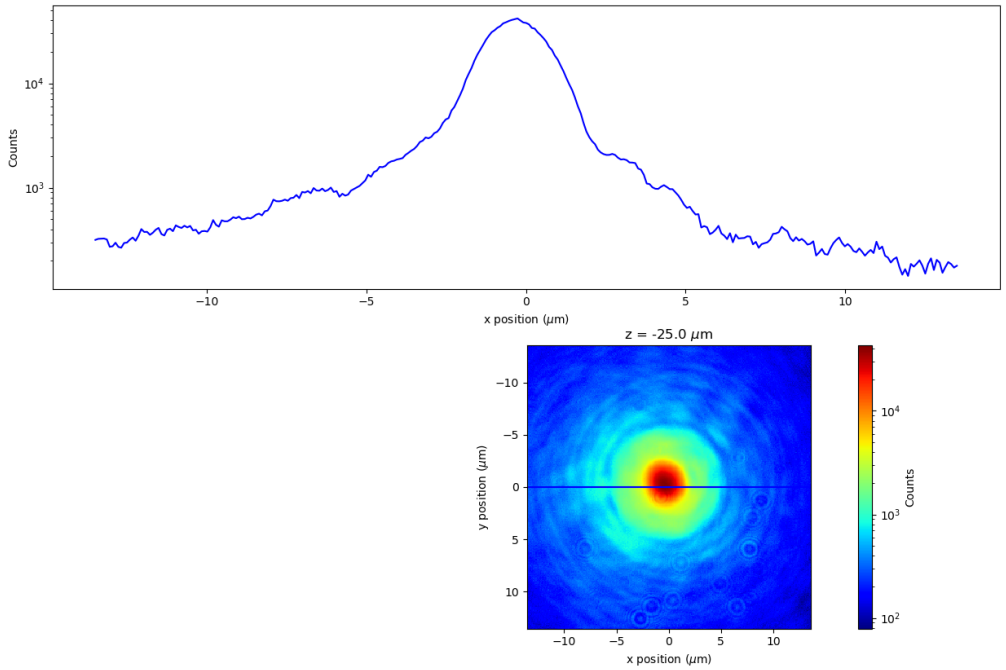


**Figure 5.10:** *A cross section of the intensity along the x and y direction (top figure). A logarithmic false-colour plot of the intensity $I(x, y)$ measured behind a close to perfect Mitutoyo 20X lens (bottom figure). Both at relative position $z = -25$ μm.*

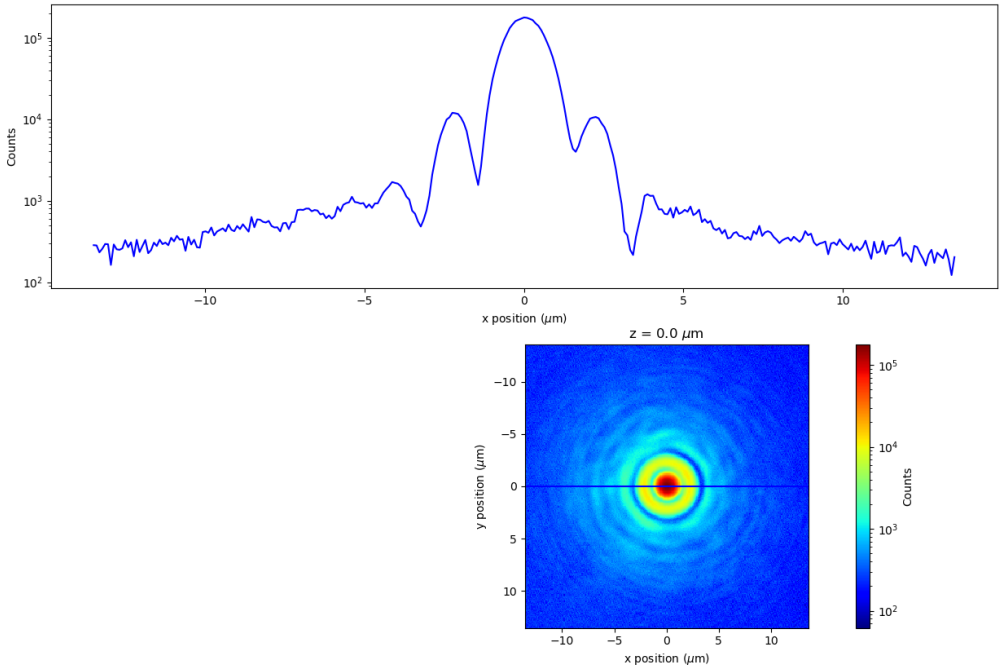


**Figure 5.11:** *A cross section of the intensity along the x and y direction (top figure). A logarithmic false-colour plot of the intensity $I(x, y)$ measured behind a close to perfect Mitutoyo 20X lens (bottom figure). Both in the focal plane ($z = 0$ µm).*

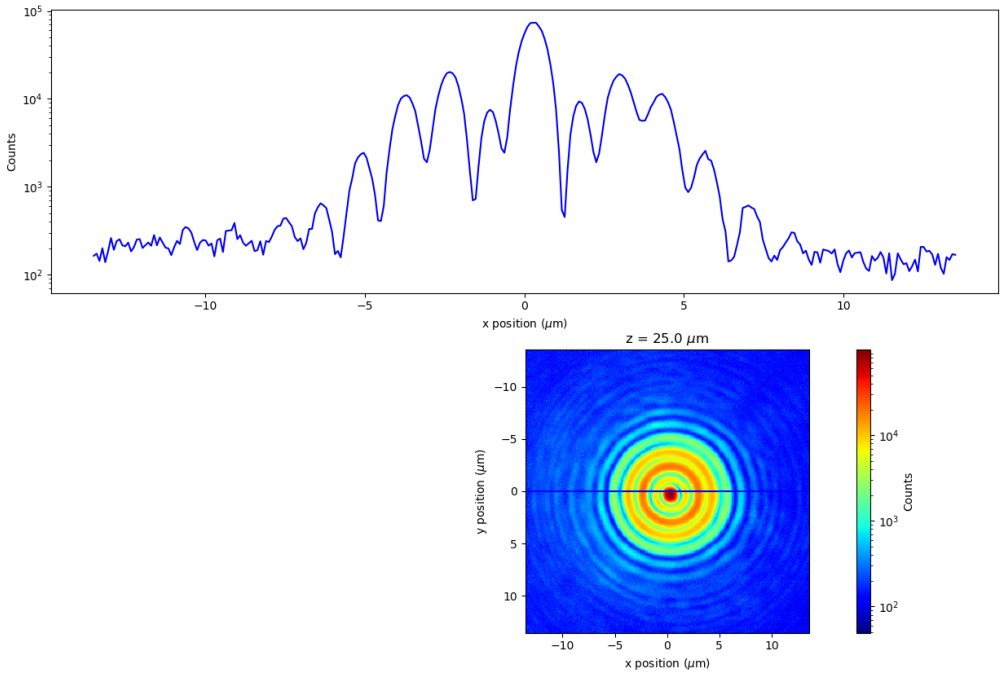


**Figure 5.12:** *A cross section of the intensity along the x and y direction (top figure). A logarithmic false-colour plot of the intensity $I(x, y)$ measured behind a close to perfect Mitutoyo 20X lens (bottom figure). Both at relative position $z = 25$ μm.*

## 5.3 Nikon 40X objective with a correction ring

The Nikon 40X objective [22] has a correction ring. By turning this ring the objective can correct for a certain amount of cover glass, which has a refractive index of 1.515 [23]. The perfect test case to see how changing the amount of spherical aberration changes the system.

We observed the focus of the fully illuminated objective. From the unaberrated focus (figure 5.13) we estimate the opening angle to be $\theta_{max} = 0.67\ (\pm 0.05)$ which gives an NA of 0.62 ($\pm$0.04) which differs by only 3% from the specified value of 0.6. The distance to the first zero in the airy pattern is estimated to be 0.7 ($\pm$0.1) $\mu$m while for a diffraction limit system this would be 0.53 $\mu$m. The system is thus close to diffraction limited (off by 32%).

The beam waist is measured (see section 3.3) to be 0.40 ($\pm$0.05) $\mu$m and the z waist is measured to be a bit smaller than 5 $\mu$m, we estimate 4.4 ($\pm$2.5) $\mu$m using a linear line between the nearest two data points. This does not reduce the error. For a Gaussian beam we know that $z_R = \pi w_0^2/\lambda$, which would give a z waist of 2.4 $\mu$m. This lies within the error on the z waist, so we cannot conclude that these parameters don't match.

We estimate the focal power fraction to be $0.74 \pm 0.15$. This is close to the perfect value of 0.771 for an Airy pattern. The pupil diameter of lens is measured to be 0.7 ($\pm$0.02) cm so the intensity amplification is then $5.7 \cdot 10^7$ ($\pm\ 2 \cdot 10^7$). This is slightly lower than for the Mitutoyo 20X lens, but this has to do with the fact that the pupil diameter is smaller (thus less light can pass through the lens). The Strehl ratio is found using the following method: First we measured the waist of Airy distribution to be about 4.6% smaller than the waist of a Gaussian distribution, so we estimate the diffraction limited waist of an Airy distribution to be

$$w_{\text{ideal}} \approx 0.95 \frac{\lambda}{\pi \text{NA}} \tag{5.5}$$

Second we use that $S \approx (F/F_{\text{ideal}})(w_{\text{ideal}}/w_0)^2$.

The Strehl ratio is estimated to be $S = 0.4 \pm 0.1$. Quite a bit lower than that of the fully illuminated Mitutoyo 20X lens.

We can repeat this analysis for the lens while setting the correction ring at 0.4, 0.8, 1.2, 1.6 and 2.0 mm (which means that the lens corrects for 0 to 2 mm cover glass with refractive index 1.515). The $I(\rho, z)$ plots for the correction ring between 0.4 mm and 1.2 mm are shown in figures 5.14 to 5.17. The images for 1.6 and 2.0 don't add anything and are thus not shown. The apparent NA is

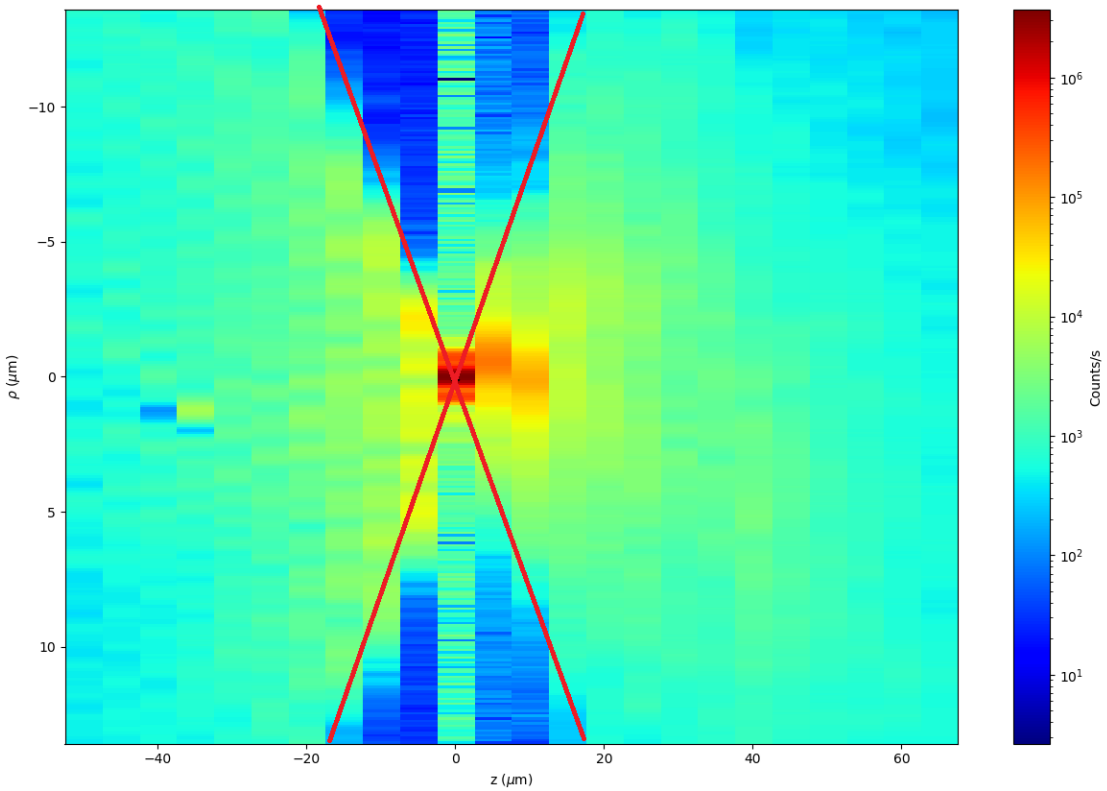


**Figure 5.13:** *A logarithmic false-colour plot of the intensity $I(\rho, z)$ measured behind a close to perfect perfect Nikon 40X lens.*

always measured in the bulls-eye region (the region with ring like structures on the negative side of the z-axis for figures 5.14 to 5.17).

The results are summarised in table 5.1. A couple of trends are noticeable: There is a lot of positive spherical aberration visible in the figures. The apparent NA quickly drops from 0.62 to 0.24 over a range of 0.8 mm and then slowly decreases to 0.20 over the range 1.2 mm to 2.0 mm. The beam waist shows the same behaviour, sharply increasing in the beginning and then slowly increasing later on. We observe that the apparent NA decreases faster than the waist increases. The z waist shows an explosive growth becoming more than 5x as large. The total focal power fraction does not seem to change much (its values are within the error margin and centred around the same values). The intensity amplification decreases, again first sharply over the first 0.8 mm and then stabilises around a mean value. The Strehl ratio is also shown and decreases. We also observe that the Strehl ratio decreases sharply from 0.40 to 0.12 over a range of 0.4 mm cover glass. The error in the NA remains nearly constant because we measure the opening angle with the same precision for all figures.

The beam waist and z waist error is completely dominated by the discretisation and as such their errors remain constant.

From this experiment we learn that introducing a small amount of spherical aberration has an enormous effect on the system, but once there is some spherical aberration introducing a bit more has less effect.

Figure 5.17 depicts the focus that the lens creates when the light passes through 1.0 ($\pm$0.2) mm (measured by hand using a ruler) of fused silica corrected for 1 mm cover glass. The thing to notice is that the amount of spherical aberration has reduced a lot. One mm glass has more spherical aberration than figure 5.15 and less spherical aberration than figure 5.16. Figure 5.17 seems to have less spherical aberration than figure 5.14. The lens corrects for microscope cover glass (which has refractive index 1.515 [23], while fused silica has refractive index 1.46 [24]) and as such over corrected for the above image. Keeping this in mind we conclude that correction ring truly corrects for a glass plate.

| Correction (mm) | Apparent NA | beam waist ($\mu$m) | z waist ($\mu$m) |
|---|---|---|---|
| 0 | $0.62 \pm 0.04$ | $0.40 \pm 0.05$ | $4.4 \pm 2.5$ |
| 0.4 | $0.32 \pm 0.05$ | $0.63 \pm 0.05$ | $7.1 \pm 2.5$ |
| 0.8 | $0.24 \pm 0.05$ | $0.75 \pm 0.05$ | $17.5 \pm 2.5$ |
| 1.2 | $0.22 \pm 0.05$ | $0.79 \pm 0.05$ | $18.8 \pm 2.5$ |
| 1.6 | $0.22 \pm 0.05$ | $0.80 \pm 0.05$ | $30.6 \pm 2.5$ |
| 2.0 | $0.20 \pm 0.05$ | $0.83 \pm 0.05$ | $25.8 \pm 2.5$ |

| Correction (mm) | $F$ | $\Omega/10^6$ | $S$ |
|---|---|---|---|
| 0 | $0.74 \pm 0.15$ | $57 \pm 18$ | $0.4 \pm 0.1$ |
| 0.4 | $0.54 \pm 0.23$ | $17 \pm 8$ | $0.12 \pm 0.05$ |
| 0.8 | $0.60 \pm 0.33$ | $13 \pm 7$ | $0.10 \pm 0.05$ |
| 1.2 | $0.58 \pm 0.33$ | $11 \pm 7$ | $0.08 \pm 0.05$ |
| 1.6 | $0.68 \pm 0.50$ | $13 \pm 10$ | $0.09 \pm 0.07$ |
| 2.0 | $0.70 \pm 0.52$ | $12 \pm 9$ | $0.09 \pm 0.07$ |

**Table 5.1:** *The characterisation values for the near perfect 40X objective at different correction values.*

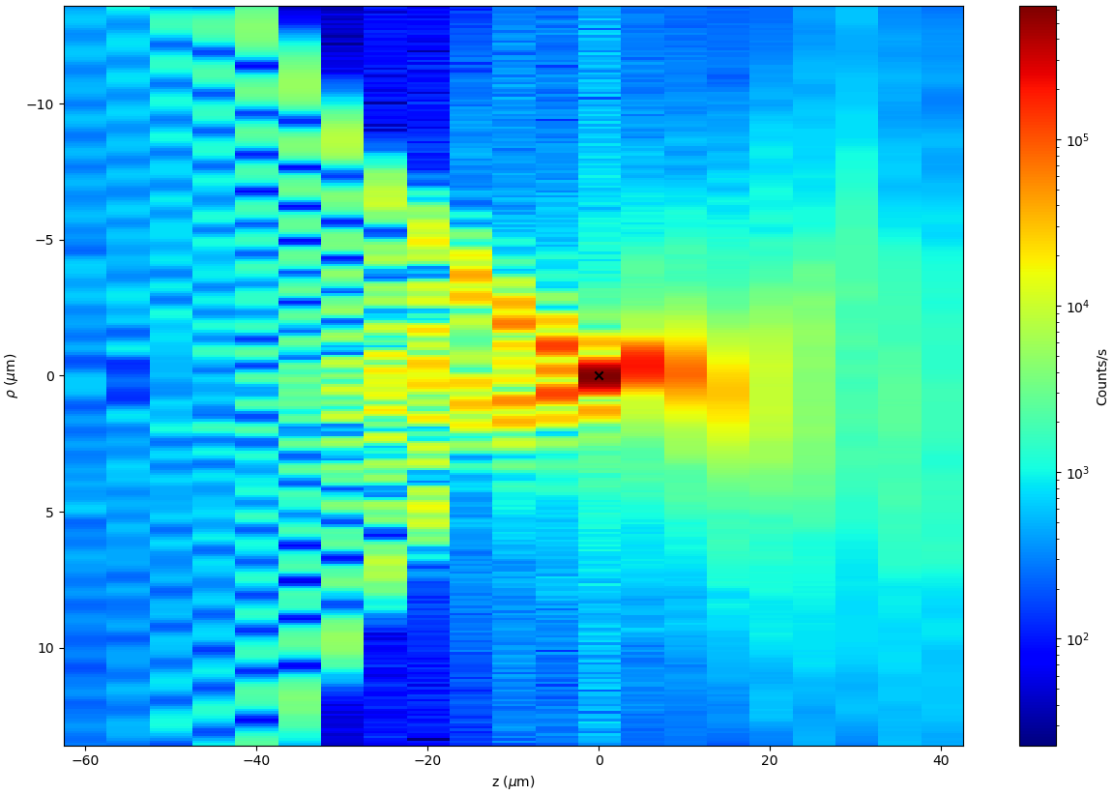


**Figure 5.14:** *A logarithmic false-colour plot of the intensity $I(\rho, z)$ measured behind a close to perfect perfect Nikon 40X lens, corrected for 0.4 mm cover glass.*

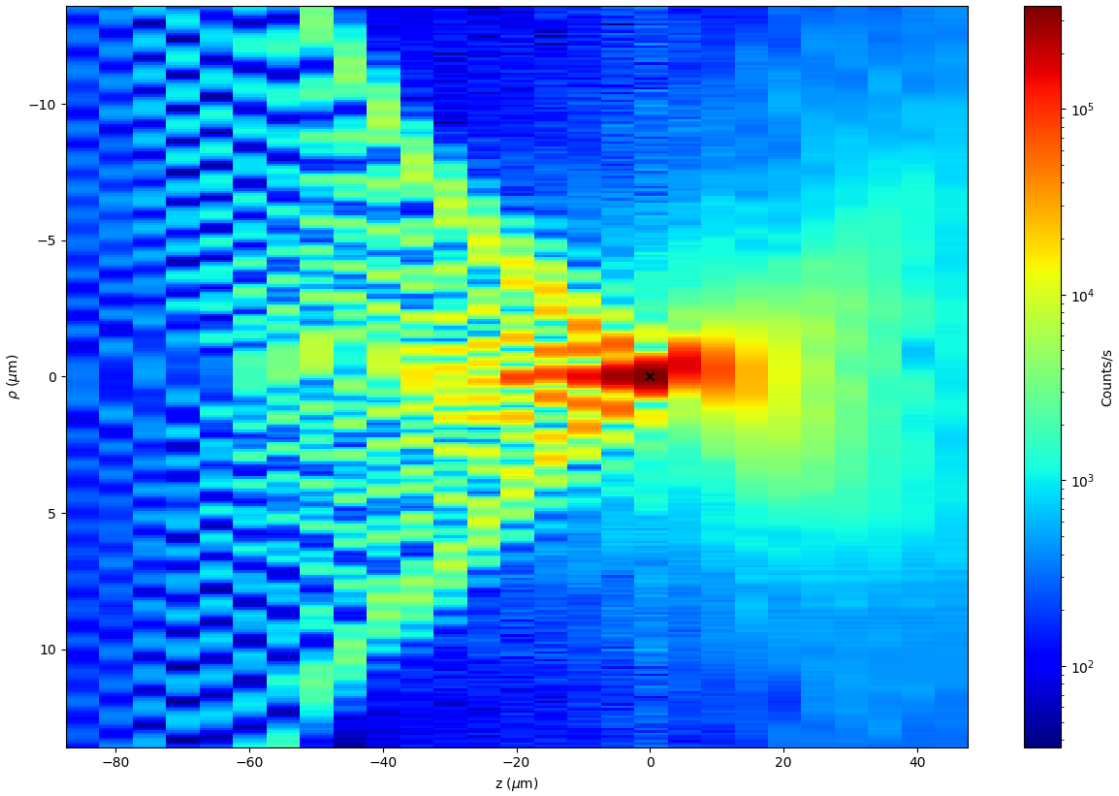


**Figure 5.15:** *A logarithmic false-colour plot of the intensity $I(\rho, z)$ measured behind a close to perfect perfect Nikon 40X lens, corrected for 0.8 mm cover glass.*

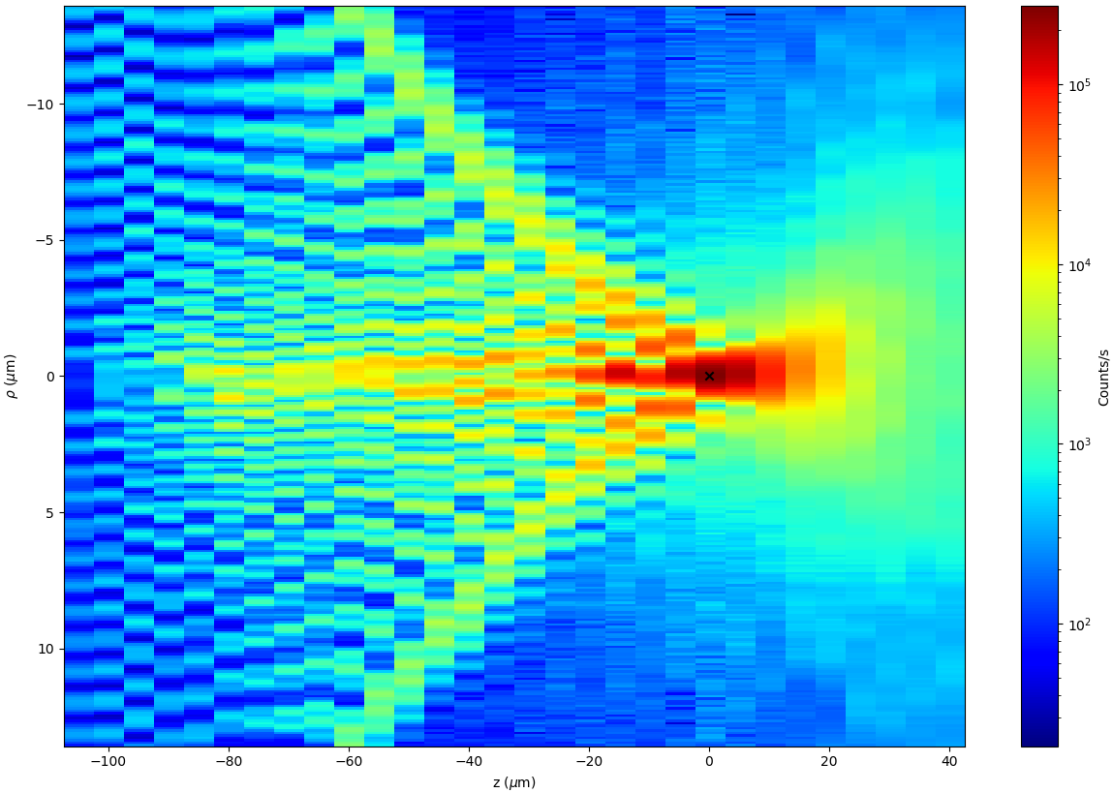


**Figure 5.16:** *A logarithmic false-colour plot of the intensity $I(\rho, z)$ measured behind a close to perfect perfect Nikon 40X lens, corrected for 1.2 mm cover glass.*

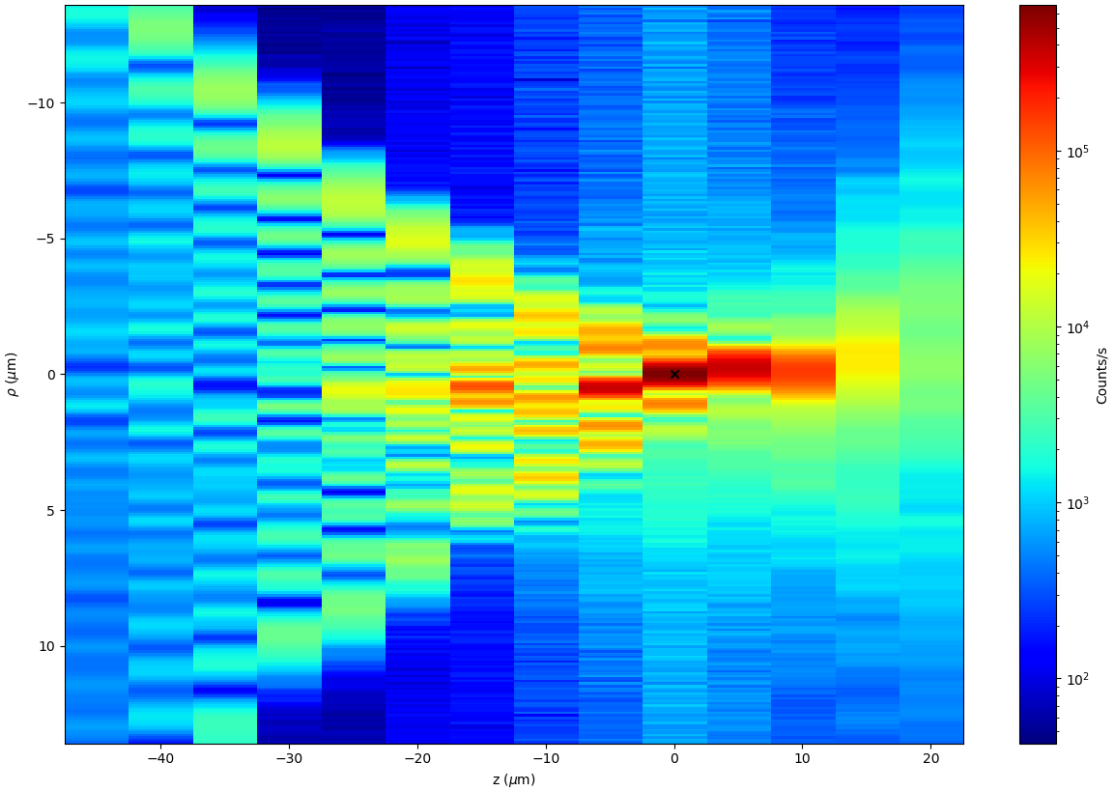


**Figure 5.17:** *A logarithmic false-colour plot of the intensity $I(\rho, z)$ measured behind a close to perfect perfect Nikon 40X lens, through 1mm fused silica with correction for 1mm cover glass.*

## 5.4 Discussion

In this chapter we analysed and characterised two near perfect lenses under various circumstances. One of the most important findings is that if there is no spherical aberration the NA one would measure from a set of CCD images will be a reasonable estimate for the actual NA. When there is spherical aberration the NA one would measure will be smaller than the actual NA. We also observed that the apparent NA decreases faster than the waist increases. We hypothesised that the apparent NA is directly linked to the amount of spherical aberration. As are the waist and Strehl ratio. The relation between the three is a research in and of itself.

Spherical aberration also changes the waist and z waist of the system meaning that the intensity profile around the focus becomes more stretched in all directions. We observed that the waist of a spherically aberrated system is much larger than than of an unaberrated system (1.5 times larger for the Mitutoyo 20X lens and 2.1 times larger for the Nikon 40X lens).

We confirmed the working of the correction ring and observed that it indeed corrected for a parallel plate. We also observed that a small amount of spherical aberration changes the system a lot. Increasing the amount of spherical aberration to an already aberrated system changes the system less.

We also observe that the spherical aberration visible for 1 mm of glass of cover glass for the 40X objective looks much worse than 6 mm fused silica does for the 20X objective (refractive index for cover glass 1.46 [23], and for fused silica 1.46 [24]). Spherical aberration introduced by a parallel plate is dependent on the NA of the beam. Comparing two objectives looking through a glass plate means that the objective with a higher NA suffers more from spherical aberrations. Future research could use equation (3.2) to quantify how spherical aberration affects systems with different NA.



Version of June 18, 2019– Created June 18, 2019 - 14:17

Chapter 6

# Characterisation of 3d printed micro-lenses

Before the characterisation, analysis or even observation of the lenses can begin, a single observation is made: the writing time of the lenses. Because the lenses were created in batches of 5 lenses we only know the total writing time, but this should still indicate the difference in writing time between galvo and piezo.
Each batch contained 5 different types of lenses: a thin lens with diameter 40 $\mu$m (radius of curvature 44 $\mu$m); a half ball lens with diameter 40 $\mu$m and height 25 $\mu$m; a thin lens with diameter 100 $\mu$m (radius of curvature 110 $\mu$m); a half ball lens with diameter 100 $\mu$m and height 60 $\mu$m; and a half ball lens with diameter 100 $\mu$m and height 140.9 $\mu$m (the focus is exactly at its backside).
In piezo mode the writing time for this batch was roughly 70 hours while in galvo mode this was 40 minutes. This means that large prints should probably be done in galvo mode, while short prints could also be done in piezo mode.

Using figure 6.2 we estimate the weak focus, that is used to illuminate the various lenses in this chapter, to have a waist of roughly 30 $\mu$m. The Intensity of this beam is averaged to 529.25 ($\pm$ 0.01) counts/s/pixel (the error was estimated by varying the area over which the intensity was averaged).

## 6.1 Half Ball lenses

We look at 4 different half ball lenses: diameter 40 $\mu$m and height 25 $\mu$m in both piezo and galvo mode; diameter 100 $\mu$m and height 60 $\mu$m in both piezo and galvo mode (see figure 4.1 for the design). The characterisation of micro-lenses begins with an optical inspection using a microscope. In figure 6.1, which was taken using an optical microscope, ring structures are visible. These structures

are formed by plateaus at different heights. The lens is printed layer by layer and thus printed in discs with decreasing width, which causes the ring structures to be visible (the darker rings are probably the edges of the disk which scatter a lot). The lens is shaped like a circular staircase. We expect that this interferes with the focusing of light and introduce additional interference effects. We expect that these half ball lenses will not behave as good lenses.

During the optical inspection the diameter of the lens was measured using the crosshairs in the eyepiece of the optical microscope. The diameter of every lens was equal to its design ($\pm 1$ $\mu$m). A set of cross sections was taken using the microscope. We estimated the height of the lens by finding the two crossections where the lens was barely in the focus of the microscope. The measured height of every lens was equal to its design (within $\pm 2$ $\mu$m).

From figure 6.1 we can also estimate the step height. The inner most disk has a diameter which is 1/6.5 of the diameter of the lens. The step height is then roughly $\Delta z \approx R(1 - \cos(1/6.5)) = 0.6$ ($\pm$ 0.1) $\mu$m. We estimated the error using various estimate of lens diameter in figure 6.1 (the edge of the outer dark grey ring is the edge of the lens). This is slightly above the indicated value of 0.5 $\mu$m

Figure 6.2 shows the back focal plane images of the 100X objective when the laser illuminates a micro-lens (top image) and when the laser does not illuminate a lens (bottom image). We used this figure to estimate the beam waist of the weak focus used to illuminate the lenses. We also use figures like this to estimate the transmissivity of the lens. We do this by calculating the power in the lens in the top image and dividing this by the power in the same area in the bottom image.

Looking at the $I(\rho, z)$ plots shown in figures 6.3 to 6.9 it is surprising how structured the foci look, the powder box and bulls-eye are easily recognisable. Their location tells us that there is negative spherical aberration in the system, that is the fused silica substrate introduces more spherical aberration than the lenses themselves. This is not strange considering that the height of the lenses are less than a fifth of the height of the substrate. The fused silica was also illuminated without a lens, which did not introduce any visible spherical aberration (the weak focus causes a flat wave front to hit the substrate). Purely from this observation we know that the half ball at least changes the light rays. The fact that a large amount of structure can be observed suggests that the lens actually works as a reasonable lens, contrary to our expectation.
When we compare figures 6.3 to 6.9 with each other, we see that the images look roughly the same. There are some important differences: The 100 $\mu$m diameter

lenses have a higher peak intensity than the 40 $\mu$m lenses; The figures seem to have the same waists and Rayleigh ranges.

The apparent NA is measured by estimating the opening angle on the side of the bulls-eye (positive side of figures 6.3 to 6.9). The beam waist $w$ is found by looking in the focal plane, finding the distance from the axis where the intensity is $e^{-2}$ of the on-axis value. The z waist is found equivalently but we consider the on-axis intensity distribution and look for the distance, from where the intensity is $e^{-2}$ of the focal on-axis intensity, to the focal plane. The focal power fraction $F$ is found by dividing the power in the focus by the power in a plane, perpendicular to the direction of propagation, far away from the focus. The intensity amplification $\Omega$ is calculated by dividing the average intensity in the focus by the average intensity of the beam illuminating the lens. The transmission $T$ is found using Back Focal Plane images (shown in figure 6.2). This is done by calculating the power within the radius of the lens if the lens is there and dividing this by the power in the same area if the lens is not there.

Table 6.1 summarises the characterisation of the four half ball lenses. The lenses appear to have the same apparent NA, which is exactly what we would expect. From equation (4.1) we know that $f \approx Rn/(n-1)$ inside the half ball lens and that $\theta_{\text{max}} \approx \arctan R/f$ so we have that:

$$\text{NA} = n \sin(\theta_{\text{open}}) \approx n_{\text{lens}} - 1 \tag{6.1}$$

The refractive index of IP-Dip is approximately 1.55 around 520 nm [12]. The NA is thus found to be roughly 0.55 ($\pm$0.01). The apparent NA that was measured for the 3d printed lenses was between 0.35 and 0.45, i.e. less than 64% and 82% of the designed value of 0.55. The diffraction limited beam waist for a half ball lens that is fully illuminated is $w = 0.95\lambda/(\pi\text{NA}) = 0.29$ $\mu$m (see equation (5.5)). If the lens is not fully illuminated (and the waist is more Gaussian) the waist increases to $w = 0.30$ $\mu$m. Because the waist of the illuminating beam is comparable to the diameter of the lenses the diffraction limited waist will lie closer to $w = 0.30$ $\mu$m. Because of this it is reasonable to approximate the diffraction limited beam as Gaussian and the diffraction limited waist as 0.30 $\mu$m.

The designed NA of a half ball lens (0.55) is comparable to the NA of the near perfect Nikon 40X lens (0.60) so we can compare the reduction in apparent NA of the half ball lenses with the reduction in apparent NA of the Nikon 40X lens at different corrections. This would allow us to make an estimate of the amount of spherical aberration that a half ball lens introduces (in terms of mm cover glass).



Version of June 18, 2019– Created June 18, 2019 - 14:17

Looking at table 5.1 we see that for 0.4 mm of cover glass, the Nikon 40X lens has a smaller apparent NA than the half ball lenses. We also estimated by eye that figures 6.3 to 6.9 show less spherical aberration than figure 5.14. We know that for an NA of 0.55 1mm of fused silica should introduce spherical aberration equal to 0.8 $\pm$ 0.2 mm of cover glass. The positive spherical aberration introduced by the half ball lenses partially compensates for the negative spherical aberration introduced by the 1 mm fused silica parallel plate. We can interpret this to mean that a half ball lens introduces an amount of spherical aberration equivalent to 0.6 $\pm$0.3 mm of cover glass.

The focal power fraction $F$ of the half ball lenses are low (0.27 to 0.45). This means that only a 27% to 45% of the light going through the lens ends up in the focus. This is still better than we expected when we looked at the shape of the lens. The z waist of the piezo written 40 $\mu$m diameter lens differs from the others (the z waist lies more than 1 standard deviation away from the values of the other samples). The focal power fraction of the piezo written 100 $\mu$m diameter lens also differs from the others. While it is likely that these are outliers, further research into micro-lenses is needed to establish why these values differ.

We can calculate the intensity amplification of a diffraction limited beam for the half ball lenses as:

$$\Omega_{\text{max}} = F_{\text{ideal, Gauss}} \left( \frac{D}{2w_0} \right)^2 \approx 0.865 \left( \frac{D}{0.60\ \mu\text{m}} \right)^2 \tag{6.2}$$

For a 40 $\mu$m diameter half ball lens this is 3.84 $\cdot 10^3$ and for a 100 $\mu$m diameter half ball lens this is 2.40 $\cdot 10^4$.

We also note that the beam waist and transmissivity of the 40 $\mu$m diameter lenses is significantly lower than that of the 100 $\mu$m diameter lenses. From this we learn that the smaller lenses perform less optimal than the larger lenses.

The difference in intensity amplification between the 40 $\mu$m and 100 $\mu$m diameter lenses can be attributed to the size of the lens. A larger lens captures more power and can thus focus more power in the same area.

What is really surprising is the large difference in transmissivity between the 40 $\mu$m and 100 $\mu$m diameter lenses. An explanation could be related to the vertical step size, because it is the same for all lenses the total number of steps is much larger for the 100 $\mu$m diameter lenses. We will try to explore this further by printing lenses using a smaller step size (see section 6.2).

We found the diffraction limited beam waist of 0.30 $\mu$m, so the measured

| Type ($\mu$m) | Apparent NA | beam waist ($\mu$m) | z waist ($\mu$m) |
|---|---|---|---|
| Galvo 40 | $0.35 \pm 0.07$ | $0.66 \pm 0.05$ | $9.0 \pm 2.5$ |
| Piezo 40 | $0.38 \pm 0.07$ | $0.67 \pm 0.05$ | $14.6 \pm 2.5$ |
| Galvo 100 | $0.45 \pm 0.07$ | $0.80 \pm 0.05$ | $11.2 \pm 2.5$ |
| Piezo 100 | $0.40 \pm 0.07$ | $0.76 \pm 0.05$ | $11.7 \pm 2.5$ |

| Type ($\mu$m) | $F$ | $\Omega$ | $T$ | S |
|---|---|---|---|---|
| Galvo 40 | $0.32 \pm 0.05$ | $67 \pm 5$ | $0.20 \pm 0.01$ | $0.017 \pm 0.001$ |
| Piezo 40 | $0.27 \pm 0.04$ | $56 \pm 5$ | $0.16 \pm 0.01$ | $0.015, \pm 0.001$ |
| Galvo 100 | $0.32 \pm 0.05$ | $230 \pm 20$ | $0.77 \pm 0.01$ | $0.010, \pm 0.001$ |
| Piezo 100 | $0.45 \pm 0.05$ | $360 \pm 30$ | $0.73 \pm 0.01$ | $0.015, \pm 0.001$ |

**Table 6.1:** *The characterisation values for the 4 half ball lenses. Type represents the writing mode and the diameter (in µm) of the lens.*

average beam waist of 0.7 ($\pm$ 0.1) $\mu$m differs by 133%. Quite a bit worse than the near perfect lenses, but still at twice the diffraction limited beam waist.

The Strehl ratio for all lenses is really low, which is exactly what we expect for these lenses. The Strehl ratio tells us that these lenses are far from perfect. The Strehl ratio of the lenses is approximately the same (except for the galvo written 100 $\mu$m diameter lens).

The intensity amplification of all lenses is higher than 1, meaning that they all improve the intensity in the focus. The highest amplification of the half ball lenses we have created is $360 \pm 30$.

The half ball lenses we created are shaped like a staircase and scatter hard at the edges and the beam waist of the focus they create is two times larger than the diffraction limited case. Yet every lens created a focus which had a smaller focus and a higher average intensity than the beam used to illuminate them. We find that when we illuminate a 3d printed half ball micro-lens with a weak focus, the lens will create a smaller focus with a higher average intensity than the beam used to illuminate it.

This means that these lenses can be used as solid immersion lenses.



Version of June 18, 2019– Created June 18, 2019 - 14:17

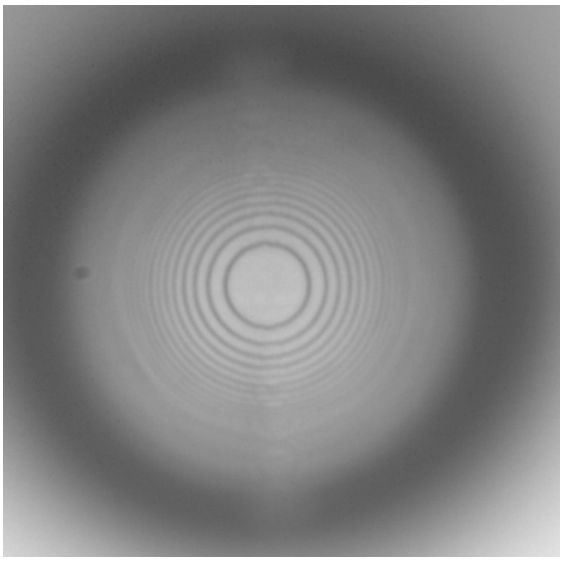

**Figure 6.1:** *An optical image of a 3d printed half ball lens with diameter 100 µm. This lens is written in piezo mode. The intensity of the input beam is* $I_0 = 529.247$ *counts/s.*



Version of June 18, 2019– Created June 18, 2019 - 14:17

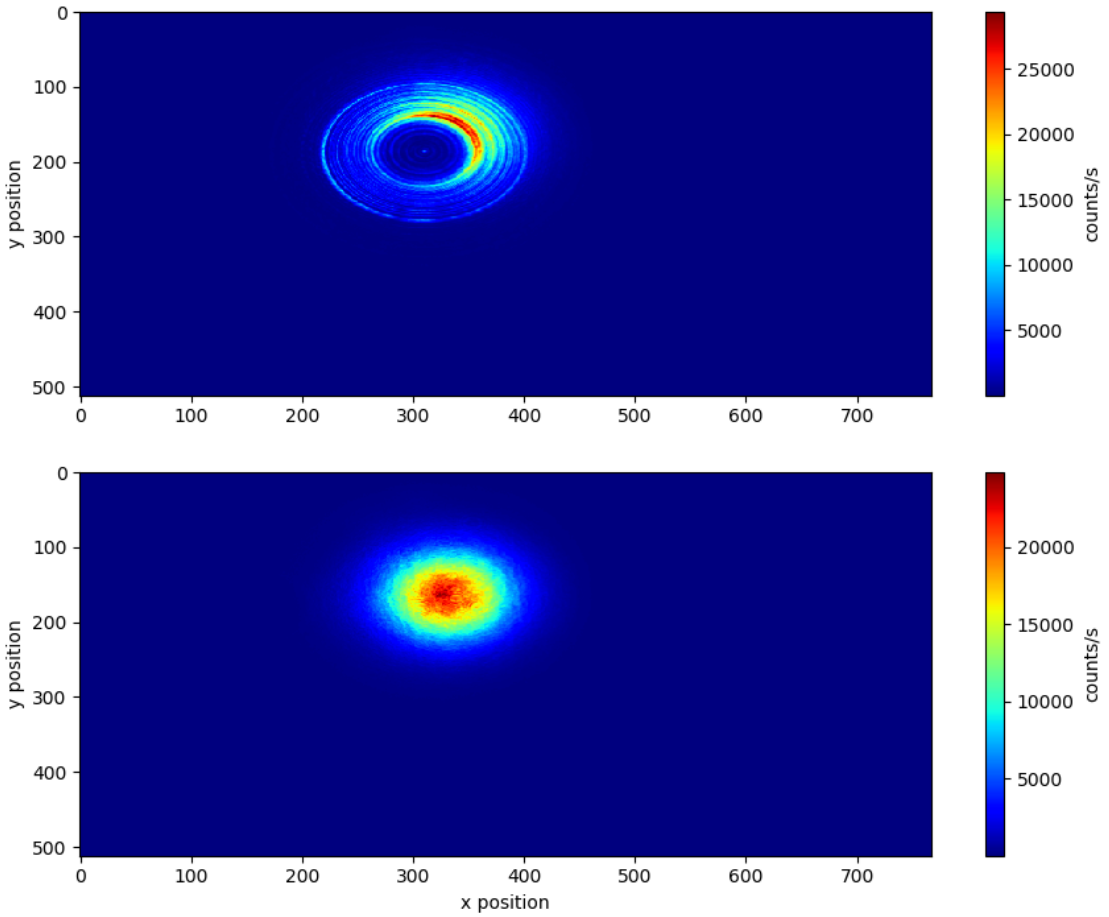


**Figure 6.2:** *A logarithmic false-colour plot of the intensity $I(x, y)$ measured in the Back Focal Plane of the Nikon 100X lens. The upper image shows the Back Focal plane with a 3d printed half ball lens with diameter 40 µm in the path of the light. The lower image shows the Back Focal Plane without the lens. The $x$ and $y$ axis are in units of pixels. These images are used to find the transmissivity.*

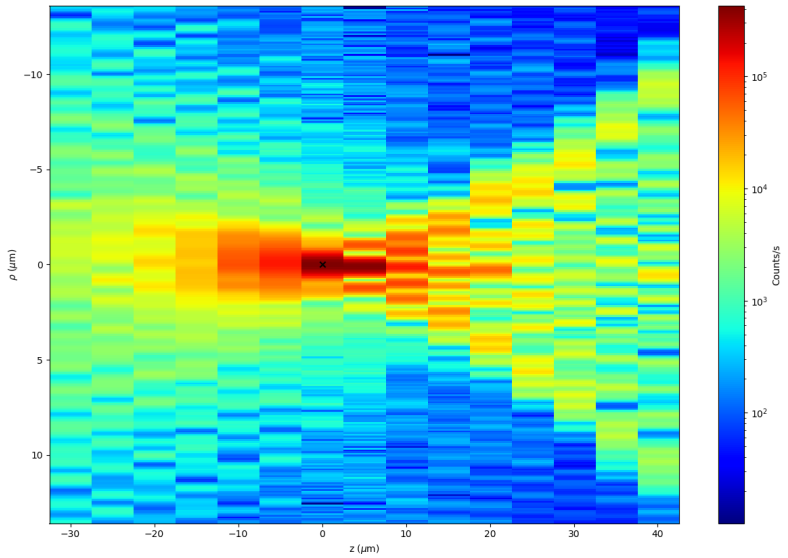


**Figure 6.3:** *A logarithmic false-colour plot of the intensity $I(\rho, z)$ measured behind a 3d printed half ball lens with diameter 100 µm. This lens is written in piezo mode.*

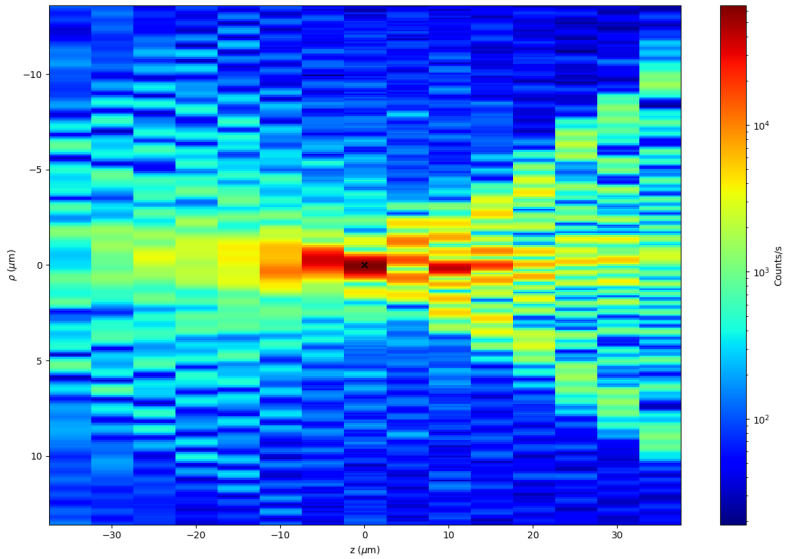


**Figure 6.4:** *A logarithmic false-colour plot of the intensity $I(\rho, z)$ measured behind a 3d printed half ball lens with diameter 40 µm. This lens is written in piezo mode.*

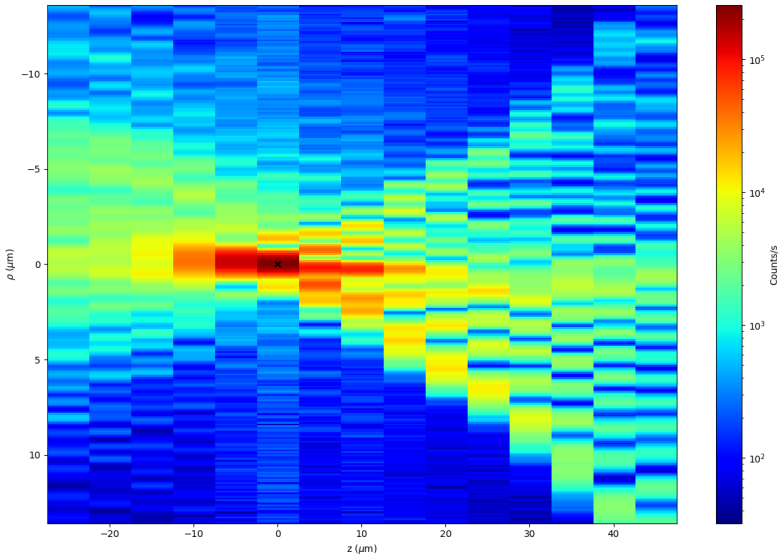


**Figure 6.5:** *A logarithmic false-colour plot of the intensity $I(\rho, z)$ measured behind a 3d printed half ball lens with diameter 100 µm. This lens is written in galvo mode.*

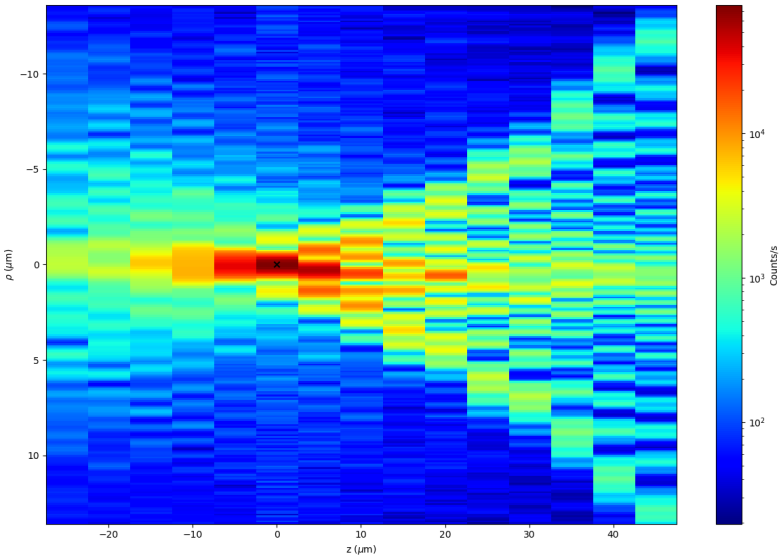


**Figure 6.6:** *A logarithmic false-colour plot of the intensity $I(\rho, z)$ measured behind a 3d printed half ball lens with diameter 40 µm. This lens is written in galvo mode.*

## 6.2 Thin lenses

We also created two bi-convex thin lenses with diameter 40 $\mu$m (in galvo and piezo mode resp.) and radius of curvature 44 $\mu$m; and 2 thin lenses with diameter 100 $\mu$m (also in galvo an piezo resp.) and radius of curvature 110 $\mu$m (see figure 4.2 for the design). Upon optical inspection of the piezo written 100 $\mu$m thin lens it showed that the print had failed (we saw a lot of connected strands of material). We hypothesise that this is because the writing time is too slow, which causes the bottom layers of the thin lens to drift before they are connected to the pillars. Because of this reason the 100 $\mu$m lenses were both excluded from the analysis.

The thin lenses are first optically inspected for faults (see figure 6.7), in this case the lens itself is free from any important obvious faults (the staircase like shape, also seen in the half ball lenses, is visible; and the missing of a single supporting pillar on the upper left side, which should not impact the lens).

Looking at the $I(\rho, z)$ plot of the piezo written thin lens (figure 6.8) we recognise the spherical aberration introduced by the fused silica plate. We observe that on the upper left side of the $I(\rho, z)$ plot there is a structure that resembles the opening angle, which seems to be equal to the opening angle on the right side. The apparent NA we get from these structures (both on the left and right) is 0.37 ($\pm$ 0.05). The opening angle of the diffraction limited system is 0.5 (the diameter and focal distance are equal). This is equal to an NA of 0.45 and a diffraction limited waist of $w = \lambda/\pi\text{NA} = 0.37$ $\mu$m. The calculated diffraction limited intensity amplification is then $2.95 \cdot 10^3$.

We compare figures 6.8 and 6.3 to figure 6.9. The lack of clear structure is the first thing we notice and we have difficulty determining the NA from figure 6.9. This lack of structure is captured by the focal power fraction which shows that a lot of the power lies outside of the focus (more than 80%). The high z waist also tells us that the on axis intensity distribution has become wider.

Even though figure 6.9 looks bad, there is still a "focus" with an increased intensity.

What is interesting is that both lenses still create a spot with a higher intensity and so we can still find the waist, focal power fraction and intensity amplification. The transmissivity can always be found. The parameters are summarised in table 6.2.

From this table one thing should be extracted: the lenses do focus the incoming light. The galvo lens (which we classify as bad) still manages to create a "focus" where the intensity is 21 times higher than the intensity of the beam that illuminates the lens.

The Strehl ratio of the piezo thin lens is better than that of every half ball lens. This is what we expected, because a perfect thin lens does not introduce spherical aberrations, while a perfect half ball lens does. The galvo lens has a lower Strehl ratio, comparible to the half ball lenses. The Stehl ratio is still low, which we can attribute to the low focal power fraction $F$, low transmissivity $T$ and high beam waist $w_0$.

The transmissivity is comparable to the half ball lenses of the same size, but the number of steps should be roughly twice as large (front and back of the thin lens). We will return to this in section 6.2.

| Type | Apparent NA | beam waist ($\mu$m) | z waist ($\mu$m) |
|---|---|---|---|
| Galvo | - | $0.94 \pm 0.05$ | $17.8 \pm 2.5$ |
| Piezo | $0.37 \pm 0.05$ | $0.90 \pm 0.05$ | $7.3 \pm 2.5$ |

| Type | $F$ | $\Omega$ | $T$ | S |
|---|---|---|---|---|
| Galvo | $0.18 \pm 0.03$ | $21 \pm 3$ | $0.15 \pm 0.01$ | $0.007, \pm 0.001$ |
| Piezo | $0.41 \pm 0.02$ | $78 \pm 10$ | $0.15 \pm 0.01$ | $0.026, \pm 0.003$ |

**Table 6.2:** *The characterisation values for the 2 thin lenses. Type represents the writing mode of the lens.*

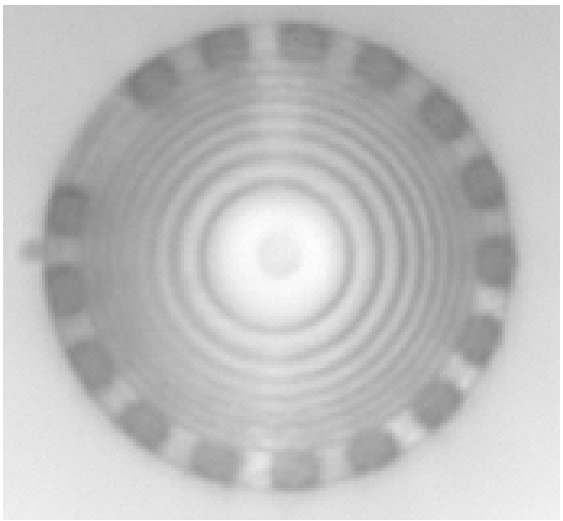

**Figure 6.7:** *An optical image of a 3d printed thin lens with diameter 40 µm. This lens is written in galvo mode. Note: one of the pillars is missing, this should not influence the working of the lens.*

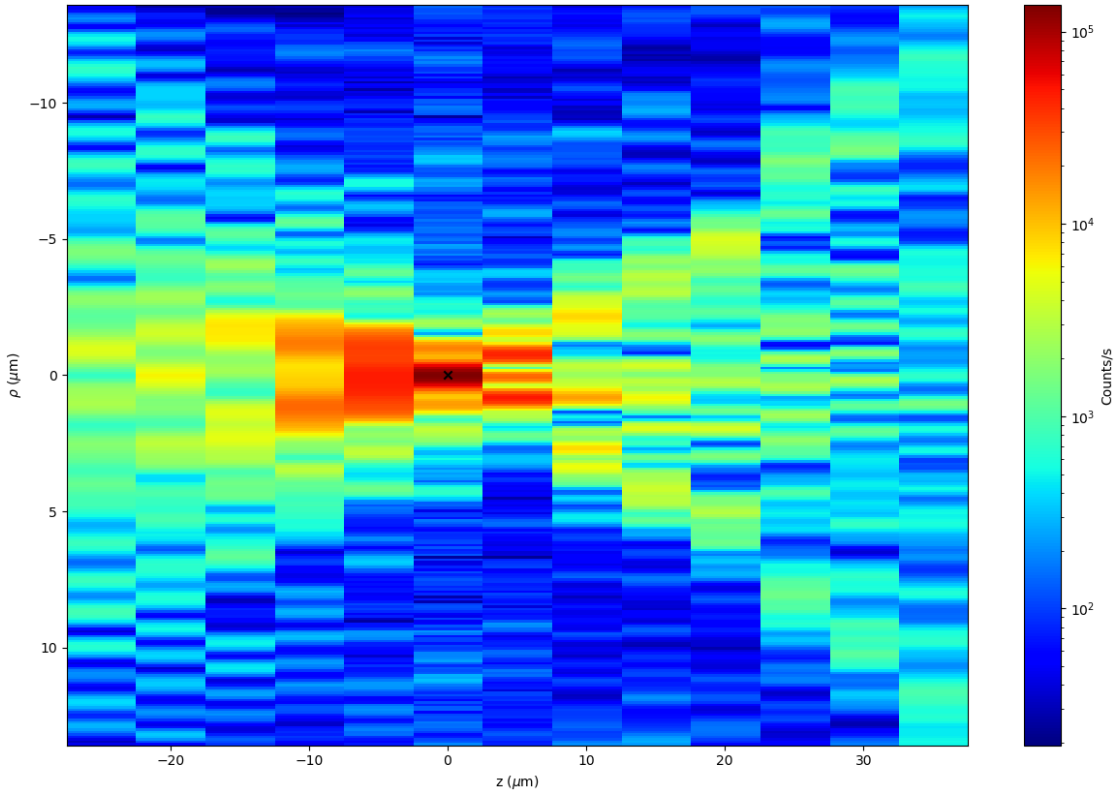


**Figure 6.8:** *A $\rho - z$ plot of a 3d printed thin lens with focal length and Diameter 40 μm. This lens is written in piezo mode.*

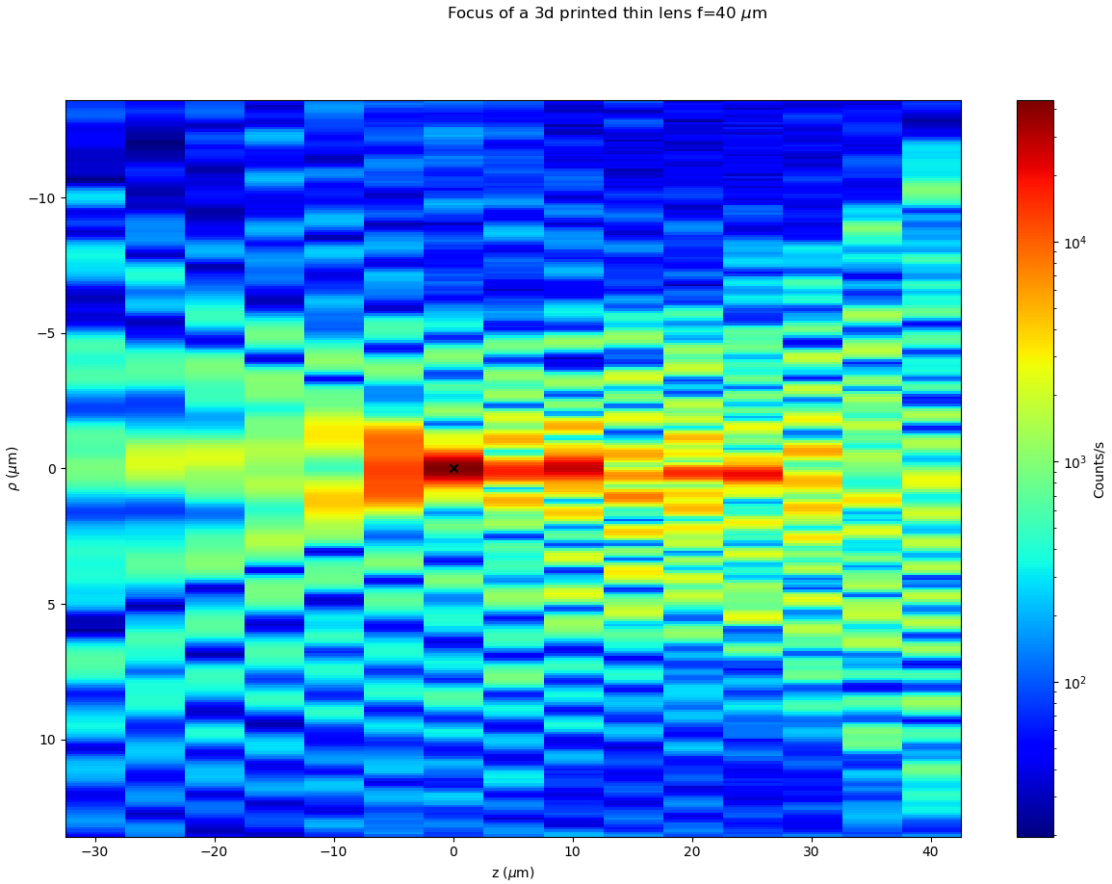


**Figure 6.9:** *A $\rho - z$ plot of a 3d printed thin lens with focal length 40 µm. This lens is written in galvo mode.*

## Smaller step size

Four lenses were printed using a 100 nm vertical step size (instead of 500 nm) using piezo writing. The exposure time that the Nanoscribe PPTG used per Voxel has not been changed. Two of these lenses were half ball lenses, the other two were thin lenses. Three of the four lenses showed defects (dark bubbles) under optical inspection, the last lens (a thin lens) did not. We are interested in the performance of a failed lens, and so we analysed one of the failed half ball lenses. The rest of the lenses have not been further analysed.

What is surprising is that a failed lens still produces a reasonable focus (figure 6.11). It is also surprising that the amount of negative spherical aberration has increased, now comparable to 0.8 mm cover glass.

From figure 6.11 we can estimate the apparent NA on the positive side (the bulls-eye) to be 0.32 ($\pm$ 0.05). This is comparable to the apparent NA found for the 40 $\mu$m diameter half ball lenses we analysed earlier (see table 6.1).

We estimate the waist to be 0.59 ($\pm$ 0.05) $\mu$m. The waist has decreased, indicating that the lens is closer to the diffraction limit.

The z waist is measured to be 10.6 ($\pm$ 2.5) $\mu$m and the focal power fraction $F$ is 0.30 $\pm$ 0.09 which is the same as we measured for the 40 $\mu$m diameter half ball lenses we analysed earlier.

The intensity amplification is 29 $\pm$ 3, quite a bit lower and the transmissivity is 0.20 $\pm$ 0.01 which is the same as measured before.

It is really surprising that this lens, which showed obvious defects under optical inspection, works almost as good as the lenses we printed before.

What one should take away from this experiment is that a vertical step size of 100 nm leads to a large number of defective products and that micro lenses with optical defects still work surprisingly well.

The physical limit in vertical step size that the Nanoscribe PPTG can use is probably near this 100 nm. A follow up research could focus on the following three topics: (i) finding this physical limit; (ii) the effect of changing the exposure time that the Nanoscribe PPTG uses to write its Voxels; (iii) finding the reason why lenses with obvious failures still focus reasonably well.



Version of June 18, 2019– Created June 18, 2019 - 14:17

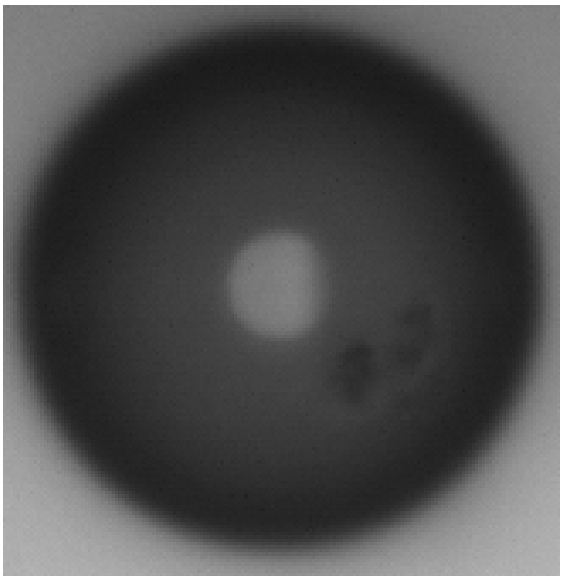

**Figure 6.10:** *Optical image of a failed half ball lens, written using a 100 nm vertical step size and in piezo. Note the defects just below and to the right of the centre of the lens (hardly visible in the figure, better visible in pdf).*

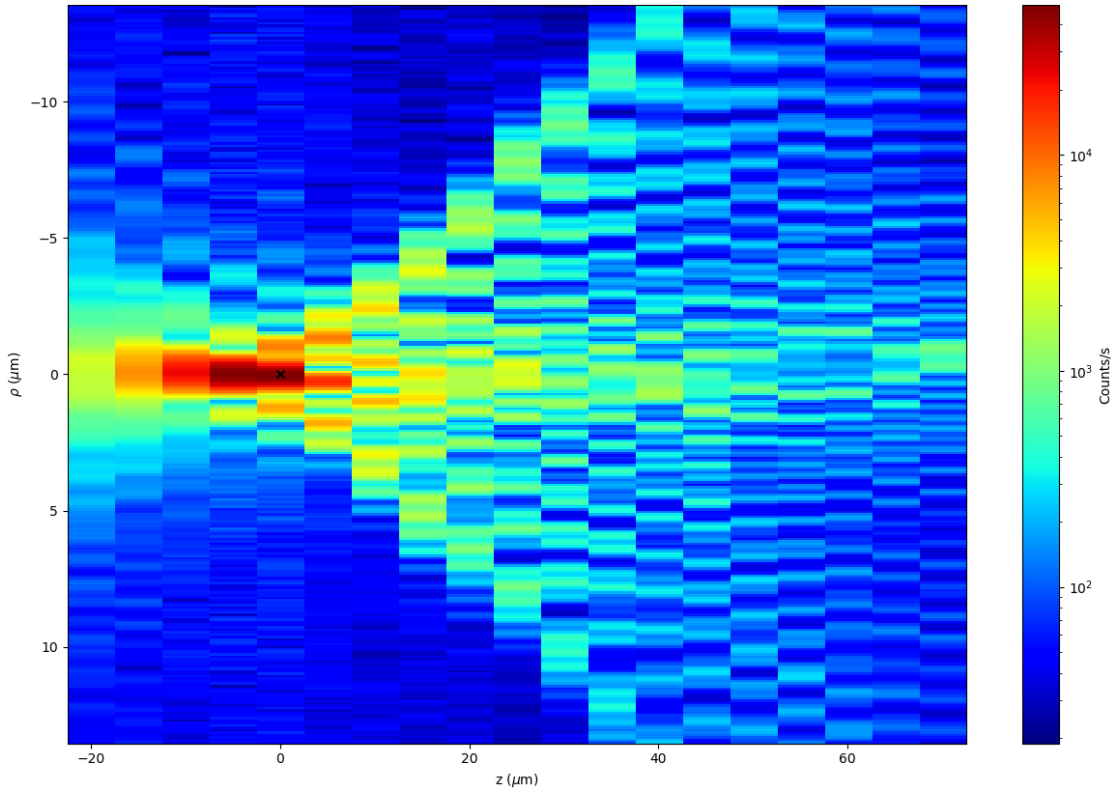


**Figure 6.11:** *Focus of a failed half ball lens, written using a 100 nm vertical step size and in piezo.*

## Determining the focal length of the 3d printed lenses.

For on unaberrated system we would estimate the focal length of the system observed in air to be $f \approx D/2\text{NA}$. The half ball lenses discussed in section 6.1 have an apparent NA that ranges between 0.35 and 0.45. If we take the NA of a half-ball lens to be 0.4 ($\pm$ 0.1) we find that the focal length of the 40 $\mu$m diameter lenses is 50 $\mu$m and the focal length of the 100 $\mu$m lenses is 125 $\mu$m. We know that the designed focal length is $f = Rn/(n-1)$, which would correspond to an observed $f = R/(n-1)$ in air. This is 36 $\mu$m for the 40 $\mu$m diameter lenses and 91 $\mu$m for the 100 $\mu$m diameter lenses. This is a difference between the estimated and designed focal length is 4 and 36 $\mu$m respectively.

The thin lens written in piezo mode in section 6.2 has an apparent NA of 0.37, if we would estimate its focal length we would get 68 $\mu$m. The designed focal length is 50 $\mu$m and so the difference between the estimated and designed focal length is 16 $\mu$m.

Our estimations of the focal lengths based on the NA are larger than the designed focal lengths. We can attribute this to the fact that spherical aberration changes the NA we measure in an $I(\rho, z)$ plot. We see that the focal lengths deviate by 4 $\mu$m for the half ball lenses with diameter 40 $\mu$m; 36 $\mu$m for the half ball lens with diameter 100 $\mu$m; and 16 $\mu$m for the thin piezo lens.

We had designed two more 100 $\mu$m diameter half ball lenses which have the following properties: the height of the lens was equal to the focal distance (like the thin lenses). We found the position of the focus (along the direction of propagation) of such a lens and compared this with the position of the focus of a normal half ball lens with diameter 100 $\mu$m that was printed on the same substrate (we changed the position of the substrate using a scanning table which means that deviations in focal position are due to the fact that the focal length is shorter).

The position of the focus was determined for the ”long” and ”short” 100 $\mu$m diameter lenses in both piezo mode and galvo mode. In piezo mode the difference between the focal lengths was 50 ($\pm$ 5) $\mu$m and in galvo it was 55 ($\pm$ 5) $\mu$m.

The difference in designed height between the ”long” and ”short” lenses was 81 $\mu$m. The focus distance is longer inside the lens and so we expect a difference of $\Delta z = \Delta h/n = 52.3$. This is exactly what we measured. These measurements do support the statement that the 2 ”long” lenses have the same change in their focus position with respect to the 2 ”short” lenses. This means that the half ball lenses have a predictable focal length, so even if the focal length does not match the designed focal length, the difference between the two is constant.

The measurements do not support any definitive statement to whether the designed focal length and the actual focal length match. Researching the actual

focal length could be done if one can identify the surface of the fused silica. We were sadly not able to do this, but further research could prove fruitful.

We can also find the Rayleigh range using the z waist $z_R = \bar{z}/\sqrt{e^2 - 1} \approx 0.40 \cdot \bar{z}$. The z waists of the 3d printed lenses all lie around 11 $\mu$m (the galvo thin lens excluded) giving a Rayleigh range of 4.4 $\mu$m. A Gaussian beam with this Rayleigh range has a beam waist of 0.85 $\mu$m (the waists of the micro-lenses are off by 10 to 20%). The Rayleigh range has a reasonable value given the beam waists that we measured. This also means that the z waist is indeed a reasonable parameter to estimate the Rayleigh range.

We made an attempt to verify if the actual focal length of the micro lenses was equal to the designed focal length. We measured that the focus position changes as expected when the height of the lens changes. From this we learn that the focal length behaves predictable. This means a large batch of lenses with the same design will have a focus length that is equal. We have not determined if the focal length is actually equal to the design and more research is needed to determine this.

## 6.3 Discussion

The analysation of the half ball and thin lenses lead to a number of surprising results. First and foremost the lenses, even though they are bad, still create a focus. The highest intensity amplification we measured is 360. The lowest intensity amplification we measured is 21, indicating that every single lens that we analysed increased the intensity in the focus.

We found that the 3d printed lenses have a beam waist that is close to diffraction limited. The smallest beam waist we measured was 0.66 $\mu$m (for a half ball lens), 2.2 times larger than the diffraction limited waist (0.30 $\mu$m). The largest beam waist was 0.9 $\mu$m (for a thin lens), 2.5 times larger than the diffraction limited waist (0.37 $\mu$m). In the discussion in section 5.4 we saw that the waist for an aberrated system is larger (we measured up to 2.1 times as large). Comparing these numbers we can conclude that the lenses, in the absence of spherical aberration, would have beam waists that are close to the diffraction limit.

A lens that showed obvious defects under optical inspection still functioned as a surprisingly good lens, increasing the intensity 29 times.

We were unable to definitively determine whether the designed focal length and the actual focal length of the micro lenses match. We observed increasing the height of a half ball lens has a predictable change in the position of the focus.

We only observed a small sample of lenses, further research should analyse the behaviour of large number of 3d printed lenses.

Chapter 7

# Conclusions and recommendations

Let us first look at the two questions that we posed at the beginning of this thesis:

1. Is it possible to design and print micro-lenses that behave predictably?

2. What are the limits, in quality, quantity and size that can be achieved?

To the first question we have a partial answer:

Yes, it is possible to print micro-lenses that create a focus. When one compares two lenses with the same designed focal length, the lenses will have the same actual focal length. The fact that different lenses with the same design have the same focal length makes the lens predictable. We expect that the actual focal length and the designed focal length match, but further research is needed to investigate this. We also observed that lenses with the same design have the same waist and transmission. We also saw that lenses written galvo and piezo are not identical, but both are of roughly equal quality.

We explored the second question less, but we did find a number of surprising results from discussion in section 6.3:

(i) The waist of the focus of the various 3d printed micro-lenses is only two times larger than the diffraction limited waist and in the absence of spherical aberration the beam waists are expected to be close to the diffraction limit. (ii) The micro-lenses do not have a smooth surface, the vertical step size and Voxel size are of order of $\lambda$. Yet these lenses have waists that are near diffraction limited. It would be interesting to research lenses whose shape is even less perfect. For now we conclude that the lenses work closer to the diffraction limit than we would expect.

The limit to the vertical step size, without changing the exposure time per Voxel, is expected to be near 100 nm. This would mean that vertical changes on the lenses can't be smaller than 100 nm which imposes a limit to the quality of the object. The vertical step size must be smaller or equal to 100 nm ($\sim \lambda/2\pi$) to produce optical components of sufficient high quality. A possibility to achieve a smaller step size would be changing the exposure time. Finding the optimal exposure time is a research of itself and could be done in the future.

No discretisation was noticed in the horizontal directions (see 6.1 and 6.7). This means that for micro-lenses the vertical step size is the important limitation to the quality. The quantity of the lenses that can be produced depends on the writing time. As noted in chapter 6 the writing time of galvo is roughly 100 times shorter (this is also what the manufacturer specifies [9]). Still it took 40 minutes to write 5 lenses in the galvo modus.
This writing time should be less than the writing time for 5 cylinders with matching diameters and height. The total volume of these cylinders is 0.1 $mm^3$ which would give an approximate upper estimate on the writing speeds. These are 0.2 $mm^3$/h for galvo and 0.04 $mm^3$/day for piezo.

The answers to the second question are: The minimum vertical step size, without changing the exposure time per Voxel, is around 100 nm, which directly limits the quality and minimal size that can be achieved. We also have an upper estimate on the writing speeds (0.2 $mm^3$/h for galvo and 0.04 $mm^3$/day for piezo) which limit the quantity that can be achieved.

In this thesis we explored a method of characterising lenses and showed the problems that arise due to spherical aberration, which include the changing of the measured (apparent) NA. This change causes the measuring of small focal lengths to be difficult. The fact that the apparent NA depends on the amount of spherical aberration surprised us. We also observed that systems with high NA suffer more from spherical aberrations. Future research can investigate whether the apparent NA can be used to quantify the amount of spherical aberration in the system. This can be done by measuring the apparent NA at increasing amounts of spherical aberration.

It is possible to quantify the amount of spherical aberration using the procedure presented in 4.3. This can be used to simulate the effects of spherical aberration on a system. Because the opening angle is one of the fit parameters, it is possible to extract the actual NA from the fit. Comparing this with the apparent NA would give an answer to the question above.

There are still some questions left open at the end of this thesis, I will men-

tion two: (i) In what ways do the printed lens and the designed lens differ? The discretisation was observed, but the focal length and NA could not be measured. One way to confirm the focal length would be to use a solid immersion lens whose focal length is exactly known and compare the absolute z-position of the solid immersion lens with a 3d printed lens.

(ii) What are the exact limits to the quality and quantity that could be achieved? A follow up research could focus on the actual limits and explore possible methods of increasing these limits.

In short, we have found that micro-lenses created with the Nanoscribe Photonic Professional GT can be used to enhance the intensity by acting as solid immersion lenses.

Chapter 8

# Appendix A: Guide to producing micro-lenses using the Nanoscribe Photonic Professional GT

In this chapter we will discuss how we designed our micro-lenses. We will do this using an example: a half ball lens with diameter 100 $\mu$m whose focus lies at its backside. We will print the lens using IP-Dip.

## 8.1 Designing a lens using Autodesk Inventor

The first step is designing the lens. We know that we want to design a half ball lens. According to equation (4.1) we know that $f \approx \frac{n}{n-1}R$. IP-Dip has a refractive index of 1.55 [12], so a half ball lens with diameter with 100 $\mu$m gives a focal length of $f = 140.9$.

Because the half ball design is rotational symmetric, we begin with designing a two-dimensional design (see figure 8.1). By revolving this design around its axis we get the full three-dimensional design (see figure 8.2). The design is exported as an .stl file. Make sure that the resolution of the .stl file is set to high (under options during exportation).

More intricate designs are possible, but are more difficult to design. More information on Autodesk inventor can be found online. Most technicians that work with 3d-printers are proficient with a design software, so it is also possible to work with them to create your design.



Version of June 18, 2019– Created June 18, 2019 - 14:17

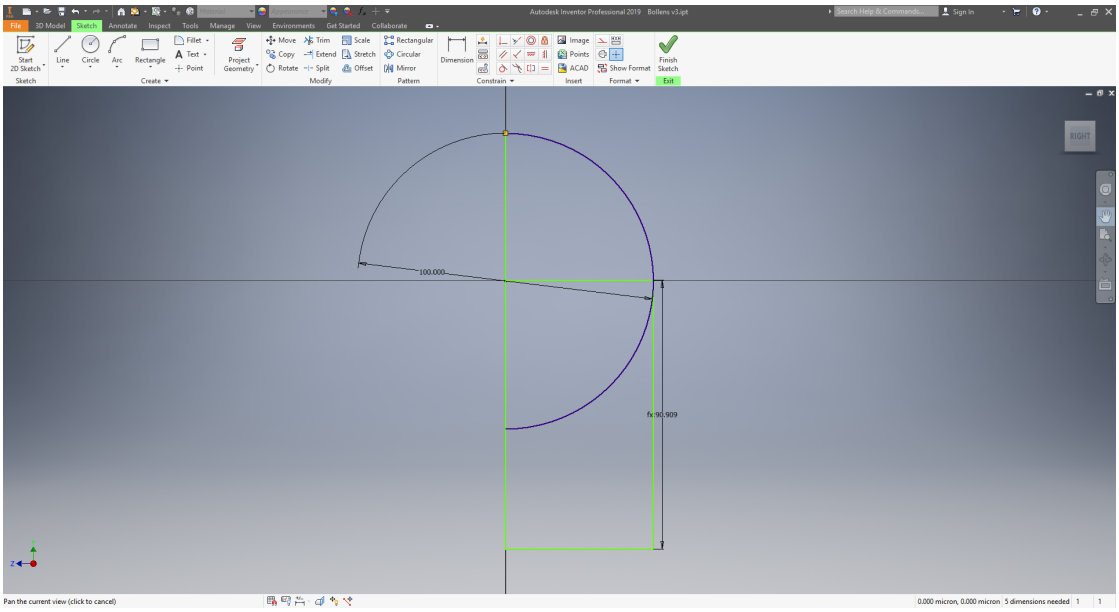


**Figure 8.1:** *The 2D design of the half ball lens with diameter 100 µm and its focus at its back side.*

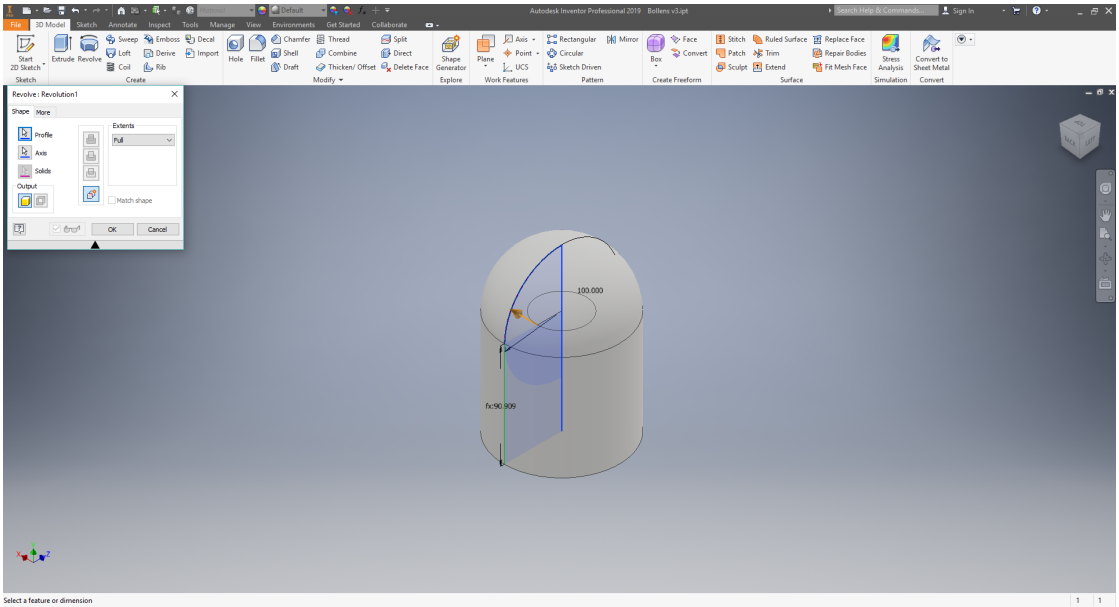


**Figure 8.2:** *The 3D design of the half ball lens with diameter 100 µm and its focus at its back side.*

## 8.2 Discretising the design using DeScribe

The created .stl file can't be printed directly. The design must first be discretised using DeScribe [7] and a number of choices must be made during this process.

We begin with choosing what *lens* to use to write our structure. We have chosen for the 63X lens, which is the best available to us.

We then choose whether to use an *adaptive* or *fixed vertical slicing mode*. The adaptive mode changes the vertical step size depending on the angle of the design. We have chosen for the fixed slicing mode, because we don't know how the adaptive mode changes between lenses. This would interfere with our characterisation (because we would have allowed an unknown free parameter). For a better slope evaluation it is advised to use the adaptive mode.

We can also choose the *slicing distance*, which sets the step size in the z direction. We will choose this to be 500 nm.

After you have chosen the lens and slicing mode, you get to choose how to fill the object.

The choice is whether to use a *solid structure* or a *sheet structure* (mostly empty). We have chosen to use the solid structure, because we think that a sheet structure will not work. It might be interesting to see if a sheet lens would work, but we expect that it won't.

The *hashing distance* is the horizontal distance between two Voxels. We used the standard choice of 0.2 $\mu$m.

The *contour count* is the number of lines that follow the contour (instead of straight lines). We have chosen not use contour lines.

The *hatching angle* rotates the writing lines of the next layer by an angle. We chose the angle to be zero.

The *base line count* is the number of layers that are not rotated before the writing lines are rotated by the hatching angle. Because we chose the angle zero, this doesn't matter.

Finally we have to choose the output.

We begin with choosing in what *mode* the structure is written. We have chosen both Piezo and Galvo, Piezo is said to be more accurate, so we will choose piezo mode for this lens.

*Hatch lines* determines if every writing line, within a single layer, is written in the same direction (from south to north) or in opposite direction (south to north, then the next line from north to south, etc.). We chose to write all line in the same direction (this allows for a slight cooling of the outer Voxels).

*Array* gives the option of printing the same object multiple times. We chose not to do this.

*Splitting mode* splits the object in multiple parts that are written one at a time. This is important for large structures, but we don't need this so we did not split our structure.

We are now done, saving our choices creates the exposure job which tells the Nanosribe PPTG what to do. For more information see the DeScribe manual [9].

## 8.3 Printing the lens

The final step is actually printing the lens. The last choice is what material to use to print our structure on. We chose to use fused silica as this is the standard choice. Because we were not personally involved in this step, we can't give you any information.
For many academics the discretising and printing steps are best done in collaboration with the technician that operates the machine.

Chapter 9

# Appendix B: Mathematical derivations

## 9.1 Power within the focus of a Gaussian beam

Let us state that we have a Gaussian beam. The radial distribution of the electric field can be interpreted as:

$$E(r) = E_0 e^{-\frac{r^2}{w^2}} \tag{9.1}$$

where $w$ is the distance from the focus such that the amplitude becomes $E_0/e$ Then the intensity distribution is simply:

$$I(r) = I_0 e^{-\frac{2r^2}{w^2}} \tag{9.2}$$

The power within the focus is defined as the integral over the intensity where $I(r) > I_0 e^{-2}$. So we can write:

$$P_{\mathrm{f}} = \frac{\int_0^{r_0} \int_0^{2\pi} I(r,\theta)\, r \sin(\theta) dr d\theta}{\int_0^{\infty} \int_0^{2\pi} I(r,\theta)\, r \sin(\theta) dr d\theta} \tag{9.3}$$

So for an ideal Gaussian beam this gives:

$$P_{\mathrm{f,\,Gauss}} = \frac{\int_0^{r_0} r e^{-\frac{2r^2}{w^2}}\, dr}{\int_0^{\infty} r e^{-\frac{2r^2}{w^2}}\, dr} \tag{9.4}$$

Using equation (9.2) and $I(r_0) = I_0 e^{-2}$ we know that $r_0 = w$ and so we can write:

$$P_{\text{f, Gauss}} = \frac{\int_0^w r e^{-\frac{2r^2}{w^2}}\, dr}{\int_0^\infty r e^{-\frac{2r^2}{w^2}}\, dr} \tag{9.5}$$

with $y = (r/w)^2$ this can be written as:

$$P_{\text{f, Gauss}} = \frac{\int_0^1 e^{-2y}\, dy}{\int_0^\infty e^{-2y}\, dy} = 1 - \frac{1}{e^2} \approx 0.86466471\ldots \tag{9.6}$$

We can also use python to estimate this by calculating the distribution and finding $w$ numerically. This is done using the following four steps:
First, generate a linear set of points used as $x$ values (we used 10 milion points between 0 and 100). Second, calculate the distributions (Gauss $y = e^{-x^2/2}$, Airy $y = 2J_1(x)/x$). Third, find where $y$ is $e^{-2}$ ($x_0$). Fourth, sum over $x \cdot y$ from 0 to $x_0$ and divide this by the total sum over $x \cdot y$.

This gives us 0.86466458 ....

For an airy pattern this method gives: 0.77106516 ....

From the comparison of the exact solution with the numerical solution we conclude that the power fraction within the focus of a Gaussian beam is roughly 86.466% and 77.107% for a beam with an airy pattern.

## 9.2 Electric Field equation for a spherically aberrated focus

Here we will derive equation (3.2):
From Fourier analysis we know that:

$$E(\vec{r}) = \iint \tilde{E}(\vec{k}) e^{i\vec{k}\cdot\vec{r}} dk_x dk_y \tag{9.7}$$

Using the rotational symmetry around the z-axis we can also write this as $\tilde{E}(\vec{k}) = \tilde{E}(\theta)$. One can argue that the polarisation scales as $\cos(\theta)\tilde{E}(\theta)$, but we essentially neglect polarisation for now.
We can write $\vec{k}\cdot\vec{r} = kz\cos(\theta) + k\rho\sin(\theta)\cos(\varphi)$ and the definition for the zeroth order Bessel function of the first kind:

$$J_0(x) = \frac{1}{2\pi}\int_{-\pi}^{\pi} e^{ix\sin(\tau)}\, d\tau = \frac{1}{2\pi}\int_0^{2\pi} e^{-ix\cos(\tau)}\, d\tau \tag{9.8}$$

Combining these together we get:

$$E(\vec{r}) = E(\rho, z) = 2\pi \int \tilde{E}(\theta) J_0(k \sin(\theta)\rho) \sin(\theta) e^{ik\cos(\theta)z}\, d\theta \tag{9.9}$$

If we consider an objective with an NA we understand that there is a limit to the integral, and we only integrate to $\theta_{\max}$. If we use Gaussian illumination it is obvious that $\tilde{E}(\theta) \sim \exp(-\theta^2/\theta^2_{\text{Gauss}})$. Spherical aberration is a defect in the phase front, which goes as $\theta^4$, so $\text{Arg}(\tilde{E}(\theta)) = \mp\pi(\theta^4/\theta^4_{\text{sphere}})$ depending in positive or negative spherical aberration. Combining all of this gives us the following integral:

$$E(\rho, z) = 2\pi \int_0^{\theta_{\max}} \tilde{E}(\theta) J_0(k \sin(\theta)\rho) \sin(\theta) e^{ik\cos(\theta)z}\, d\theta \tag{9.10}$$

with $\tilde{E}(\theta) = E_0 e^{-\frac{\theta^2}{\theta^2_{\text{Gauss}}} \mp \pi \frac{\theta^4}{\theta^4_{\text{sphere}}}}$ Now we can absorb the $2\pi$ into the $E_0$, reintroduce the polarisation, and write $q = \sin(\theta)$

$$E(\rho, z) = \int_0^{q_{\max}} \tilde{E}(q) J_0(kq\rho) q e^{ikz\sqrt{1-q^2}}\, d\theta \tag{9.11}$$

We use the approximation that we can write $\tilde{E}(q) = E_0 e^{-\frac{q^2}{q^2_{\text{Gauss}}} \mp \pi \frac{q^4}{q^4_{\text{sphere}}}}$ finally giving us:

$$E(\rho, z) = E_0 \int_0^{q_{\max}} q J_0(kq\rho) e^{-\left(\frac{q}{q_{\text{Gauss}}}\right)^2 - i\left(\pm\pi\left(\frac{q}{q_{\text{sphere}}}\right)^4 - kz\sqrt{1-q^2}\right)}\, dq \tag{9.12}$$

## 9.3 Focal length of a half ball lens

A half ball Lens with radius $R$, refractive index $n_{\text{lens}}$ surrounded by a medium with refractive index $n_{\text{medium}}$ is illuminated by a parallel beam. Snell's law states that:
The angle of a light ray with respect to the normal of the lens $\theta_{\text{medium}}$ is equal to the angle between the direction of the parallel beam and the radius to a on the surface at height $r$ .

$$\sin(\theta_{\text{medium}}) = \frac{r}{R} \tag{9.13}$$

Using figure 9.1 and the sine rule we get the following relation:

$$\frac{\sin(\theta_{\text{lens}})}{x} = \frac{\sin(\pi - \theta_{\text{medium}})}{s} \tag{9.14}$$



Version of June 18, 2019– Created June 18, 2019 - 14:17

with $x$ equal to $f(r) - R$ and $s$ the path of the light through the lens to the focus, which is equal to: $s = \sqrt{r^2 + (f(r) - \delta)^2}$. $f(r)$ is the focal distance (taken from the front of the lens to where the light crosses the optical axis). We also know that $\sin(\pi - \theta) = \sin(\theta)$ and so we get:

$$s \sin(\theta_{\text{lens}}) = x \sin(\theta_{\text{medium}}) = xn \sin(\theta_{\text{lens}}) \tag{9.15}$$

where we used Snell's law ($\sin(\theta_{\text{medium}}) = n \sin(\theta_{\text{lens}}), n = n_{\text{lens}}/n_{\text{medium}}$). This gives:

$$s = xn \tag{9.16}$$

$$r^2 + (f(r) - \delta)^2 = n^2 (f(r) - R)^2 \tag{9.17}$$

using that $(R - \delta)^2 + r^2 = R^2 \Rightarrow \delta = R - \sqrt{R^2 - r^2}$ we can solve for $f(r)$:

$$n^2 (f(r) - R)^2 = r^2 + (f(r) - R + \sqrt{R^2 - r^2})^2 \tag{9.18}$$

After some calculus it becomes obvious that:

$$f(r) = R + \frac{\sqrt{R^2 - r^2}}{n^2 - 1} \left( 1 \pm \sqrt{\frac{n^2 R^2 - r^2}{R^2 - r^2}} \right) \tag{9.19}$$

The positive branch must yields the correct results in the limit of $r \to 0$ so:

$$f(r) = R + \frac{\sqrt{R^2 - r^2}}{n^2 - 1} \left( 1 + \sqrt{\frac{n^2 R^2 - r^2}{R^2 - r^2}} \right) \tag{9.20}$$

For small radii we can taylor expand this into:

$$f(r) = \frac{n}{n-1} R \left( 1 - \frac{1}{2n^2} \left( \frac{r}{R} \right)^2 + \dots \right) \tag{9.21}$$

## 9.4 Focal distance change introduced by a parallel plate

A light ray at a distance $r$ from the optical axis enters a parallel plate at an angle $\theta$. If we call the thickness of the plate $d$, the original focal distance from the front of the plate $a$, the new focal distance from the back of the plate $c$ and the height at which the ray leaves the plate $r - b$ we see the following relation $a + \Delta f =$

$c + d$. There is also the following relations $\tan(\theta) = r/a$, $\tan(\theta) = (r-b)/c$ and $\tan(\theta_2) = b/d$. This gives:

$$\Delta f = c - (a - d) = d + \frac{r-b}{\tan(\theta)} - \frac{r}{\tan(\theta)} = d\left(1 - \frac{\tan(\theta_2)}{\tan(\theta)}\right) \tag{9.22}$$

Snell's law says that $\sin(\theta) = n\sin(\theta_2)$ so we can write:

$$\Delta f = d\left(1 - \frac{\cos(\theta)}{n\cos(\theta_2)}\right) \tag{9.23}$$

Using the relation that $\cos(\arcsin(x)) = \sqrt{1-x^2}$ we get that

$$\Delta f = d\left(1 - \frac{\cos(\theta)}{n\sqrt{1 - \left(\frac{\sin(\theta)}{n}\right)^2}}\right) \tag{9.24}$$

$$\Delta f = d\left(1 - \frac{\cos(\theta)}{\sqrt{n^2 - \sin^2(\theta)}}\right) \tag{9.25}$$

In the limit of $\theta = 0$ we can taylor expand this to:

$$\Delta f \approx d\frac{n-1}{n}\left(1 + \frac{n+1}{2n^2}\theta^2 + \dots\right) \tag{9.26}$$



Version of June 18, 2019– Created June 18, 2019 - 14:17

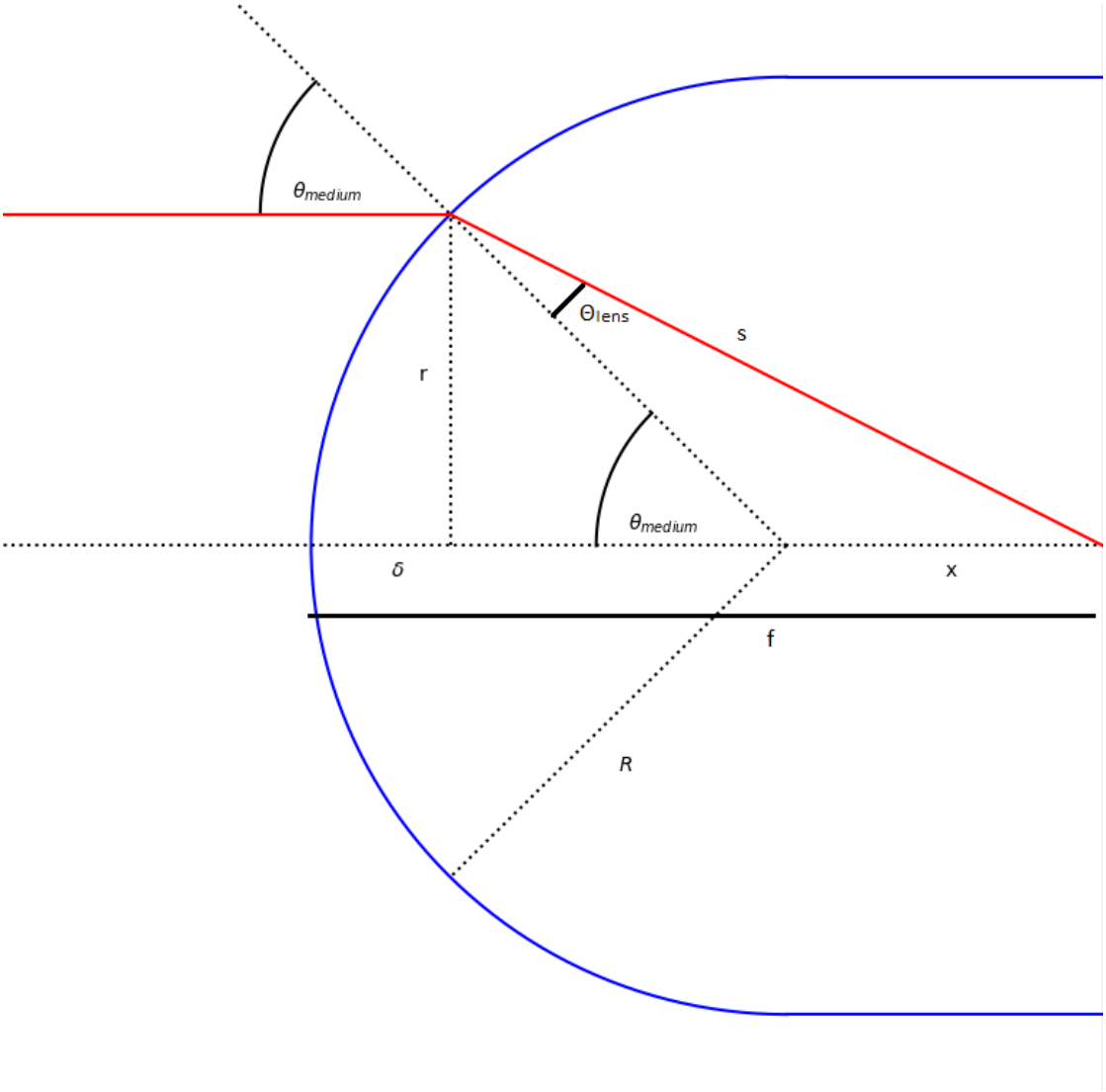


**Figure 9.1:** *A light ray at a distance r of the optical axis going through a half ball lens. The figure also shows a number of used variables.*

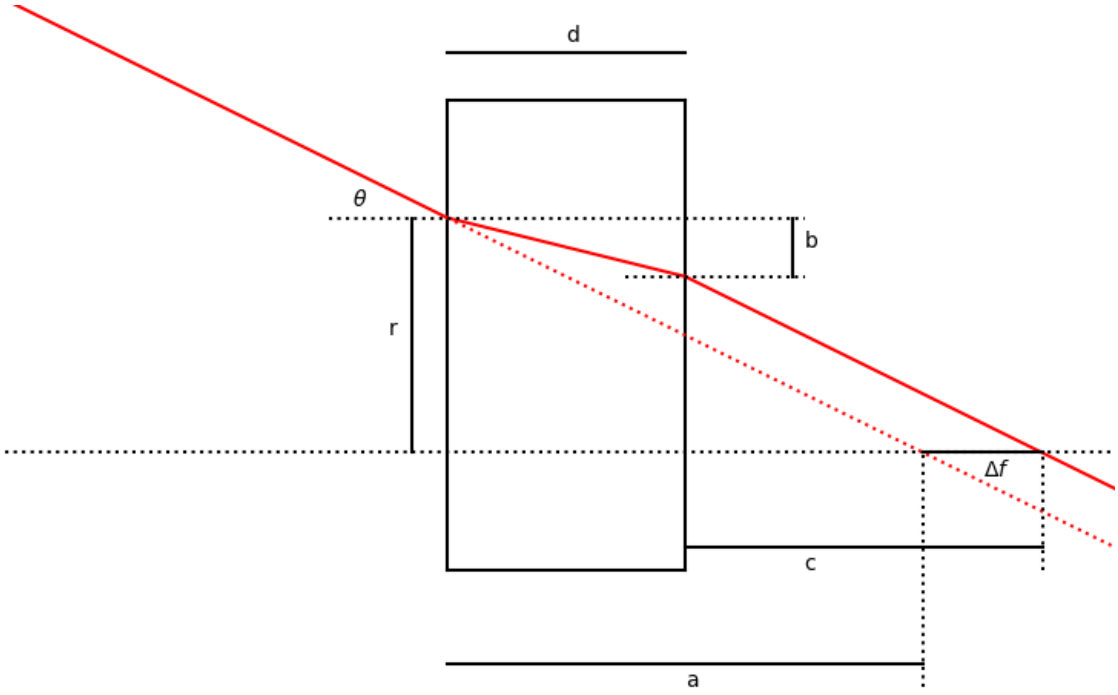


**Figure 9.2:** *A light ray hitting the parallel plate at an angle θ.*

# Bibliography


[1] A. Gurdita, *5 Most Promising 3D Printed Organs for Transplant*, (2018), Retrieved from https://all3dp.com/2/5-most-promising-3d-printed-organs-for-transplant/.

[2] *3Dprintedhouse website*, Retrieved from https://www.3dprintedhouse.nl/nl/.

[3] T. Hoffman, *3D printing: What you Need to Know*, (2018), Retrieved from https://www.pcmag.com/article/289175/3d-printing-what-you-need-to-know.

[4] M. von Uble, *3D Printing Materials - All You Need to Know in 2019*, (2019), Retrieved from https://all3dp.com/1/3d-printing-materials-guide-3d-printer-material/.

[5] *123-3d website*, Retrieved from https://www.123-3d.nl/3D-printers-p1603.html.

[6] M. Zhou, *3D printed gun controversy: Everything you need to know*, Retrieved from https://www.cnet.com/news/the-3d-printed-gun-controversy-everything-you-need-to-know/.

[7] *Nanoscribe website*, https://www.nanoscribe.de/en/, https://www.nanoscribe.de/en/downloads/ and https://www.nanoscribe.de/en/products/software/.

[8] A. Ostendorf and B. N. Chichkov, *Two-Photon Polymerization: A New Approach to Micromachining*, (2006), Retrieved from https://www.photonics.com/Articles/Two-Photon_Polymerization_A_New_Approach_to/a26907.

[9] *Describe: Getting started Manual*, https://cmi.epfl.ch/photo/files/Nanoscribe/Describe.manual.pdf.

[10] J. Clayden, N. Greeves, and S. Warren, *Organic Chemistry*, Oxford, England: Oxford University Press, 2 edition, 2012, Chapter 37.

[11] R. W. Boyd, *Nonlinear Optics*, San Diego, California, USA: Academic Press, Inc., 1992, Page 16.

[12] S. Dottermusch, D. Busko, M. Langenhorst, U. W. Paetzold, and B. S. Richards, *Exposure-dependent refractive index of Nanoscribe IP-Dip photoresist layers*, Opt. Lett. **44**, 29 (2019), At $\lambda = 520$ nm, $n \approx 1.55$. Fig. 4 for Two-Photon Polymerisation.

[13] A. Small, *Spherical aberration, coma, and the Abbe sine condition for physicists who don't design lenses*, American Journal of Physics **86**, 487 (2018).

[14] O. Svelto, *Principles of Lasers*, New York, NY, USA: Springer, 4 edition, 1998, Page 152.

[15] V. N. Mahajan, *Optical Imaging and Aberrations Part II. Wave Diffraction Optics.*, Bellingham, Washington, USA: SPIE - The International Society for Optical Engineering, 1998.

[16] V. N. Mahajan, *Optical Imaging and Aberrations Part I. Ray Geometrical Optics.*, Bellingham, Washington, USA: SPIE - The International Society for Optical Engineering, 1998.

[17] *Autodesk website*, https://www.autodesk.nl/.

[18] *AR-Coated Single Mode Fiber Optic Patch Cables*, https://www.thorlabs.com/newgrouppage9.cfm?objectgroup_ID=1792.

[19] S. Stallinga, *Finite conjugate spherical aberration compensation in high numerical-aperture optical disc readout*, Appl. Opt. **44**, 7307 (2005).

[20] *Github Repository containing the CCD reduction python files.*, https://github.com/characterisation-micro-lenses/CCD-Reducer.

[21] *Mitutoyo 20x objective*, https://www.edmundoptics.com/p/20x-mitutoyo-plan-apo-nir-infinity-corrected-objective/6834/.

[22] *Nikon 40x objective*, https://www.edmundoptics.eu/p/40x-objective-nikon-cfi-super-fluor/30635/.

[23] *MicroscopyU, Adjustment of Objective Correction Collars*, `https://www.microscopyu.com/tutorials/adjustment-of-objective-correction-collars`.

[24] I. H. Malitson, *Interspecimen Comparison of the Refractive Index of fused silica.*, J. Opt. Soc. Am. **55**, 1205 (1965), At $\lambda = 520$ nm, $n \approx 1.46$.